Determination Of Systematic Uncertainities For The Measurement of the $t\bar{t}\gamma$ Cross Section with ATLAS

M A S T E R A R B E I T

zur Erlangung des akademischen Grades
Master of Science
(M.Sc.)

der Naturwissenschaftlich-Technischen Fakultät
-Department Physik-
der Universität Siegen

vorlgelegt von
Naim Bora Atlay

im Oktober 2011

Contents

List of Figures

List of Tables

Chapter 1

Introduction

It would not be an exaggeration to say that a new epoch has begun in particle physics since the experiments at the LHC have begun to take physics data. The LHC has already collected data equivalent to 5 fb^{-1} of integrated luminosity and will provide much more data during the next years. Previous collider experiments have obtained excellent results, but the standard model is not completely verified by the earlier experiments. The LHC will provide a great opportunity to complete the missing pieces in the picture of modern particle physics.

The main purpose for the LHC and its experiments is to conclude the search for the Higgs boson. Although the Higgs boson was theoretically hypothesized in 1964 [1, 2], it has still not been experimentally observed. Besides the Higgs boson, the search for particles beyond the standard model is of great importance for the scientists at the LHC and LHC experiments. One example of such particles are the supersymmetric partners of standard model particles. Another significant research topic at the LHC is top quark physics. Due to its large mass, it could not be observed until 1995, even though it was postulated in 1973 [3]. However, since the observation, the properties of the top quark have not been fully determined. One of its significant properties is its mass. It's known that both W boson and top quark masses give hints to the Higgs boson mass. Other studies on top quark properties are its electric charge, W helicity in top quark decay, spin correlation and asymmetry in strong $t\bar{t}$ production and radiative top quark processes $t\bar{t}\gamma$.

One of the keystones of today's particle physics is the event simulation, utilising Monte Carlo (MC) event generators. It would not be possible to design these experiments and perform analyses without MC generators. However, there are still some points where they are not fully sufficient. As it is subject of this thesis, in the $t\bar{t}\gamma$ analysis, the calculations used to produce the signal sample are performed at leading order. Leading order calculations provide a good estimate for the cross section of the process, but it is still insufficient. A more precise analysis would be guaranteed by using a next-to-leading order sample, but production of a next-to-leading order $t\bar{t}\gamma$ sample is not available yet, although its theoretical calculations exist [4]. In absence

of a next-to-leading order $t\bar{t}\gamma$ sample, it is reasonable and needed to implement a systematic uncertainty, which should cover the uncertainty of leading order event generation.

In this thesis, a determination of this uncertainty is performed. First, an overview of the ATLAS experiment will be given. Then, basics of the standard model and properties of top quarks will be discussed. Then, the phases of data simulation will be described step by step, starting from the event generators, till the final data format. Details of the event generation will be described separately in Chapter 4. Chapter 5 will present the strategy and the results of uncertainty determination due to the event generation using leading order calculations. Finally, the last chapter will summarize the thesis and give an outlook.

Chapter 2

The ATLAS Experiment at the LHC

The ATLAS (A Torodial LHC Apparatus) detector is currently the largest and one of the most intricate particle detectors. It is constructed as one of the four main detectors of the Large Hadron Collider. This high-performance particle accelerator is a proton-proton collider, which is located on the border of Switzerland and France, at CERN (le Conseil Européen pour la Recherche Nucléaire) near Geneva. With the designed center of mass energy of $\sqrt{s} = 14$ TeV, the LHC provides the opportunity to search for new physics beyond the standard model as well as to perform more precise measurements for previously determined Standard Model parameters of until now inaccessible energy scales. The LHC operates at a center-of-mass energy of 7 TeV for the time being.

As a consequence of a technical problem[5], the LHC has started to operate approximately fourteen months later, in November 2009, than the scheduled running period and has recorded its first collision [6, 7]. Since then the LHC has recorded data with more than 5 fb^{-1} of integrated luminosity. For comparison, the Tevatron $p\bar{p}$ collider at Fermilab Laboratory in Chicago has collected 11 fb^{-1} integrated luminosity of data in approximately fifteen years [8]. The LHC will run through to the end of 2012 with a short technical stop at the end of 2011. The beam energy for 2011 is 3.5 TeV. With this schedule, the LHC's experiments have a good chance of finding new physics within the next two years, before the LHC goes into a long shutdown to prepare for higher energy running starting 2014 [9].

2.1   The Large Hadron Collider

The LHC [11] is built in a 27 km long circular tunnel which was originally constructed for the LEP accelerator. The tunnel is located in a depth between 50 m and 175 m below the Earth's surface. The LHC accelerates bunches of up to 10^{11} protons and collides them with a design center of mass energy of $\sqrt{s} = 14$ TeV in four designed collision points. ATLAS[12] is installed at point 1, ALICE [13] at point 2, CMS [14] at point 5 and LHCb [15] at point 8. The two large multipurpose detectors ATLAS
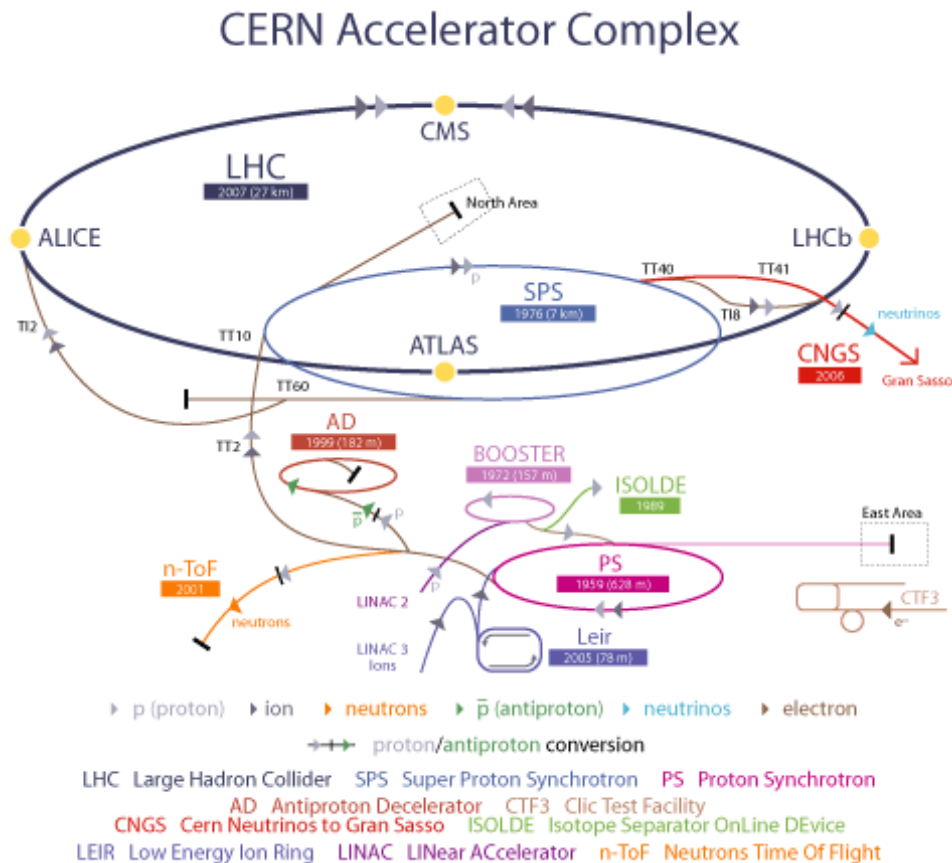
Figure 2.1: Protons are obtained by removing electrons from hydrogen atoms. They are injected from the LINAC2 into the PS Booster, then the PS, followed by the SPS, before finally reaching the LHC. Protons will circulate in the LHC for 20 minutes before reaching the maximum speed and energy. [10]

and CMS were built aiming at the discovery of the Higgs boson and of new physics beyond the standard model. One of the other two midsized detectors, LHCb, is dedicated to B-physics and CP violation while the other, ALICE, probes the results of heavy ion collisions of the LHC programme.

Before the injection of protons into the LHC, the protons are pre-accelerated through a pre-accelerator setup. Firstly, the protons gain a kinetic energy of 50 MeV in the LINAC2(LINear particle ACcelerator) and then are accelerated up to 1.4 GeV in the PSB (Proton Synchroton Booster) and as the third step up to 26 GeV in the PS(Proton Synchroton). In the final stage the SPS (Super Positron Synchroton), just before the ring of LHC, the protons reach 450 GeV.

The magnetic field intensity in the LHC magnets to conserve beam intensity and to keep the protons on their circular path is obtained by using superconducting magnets which provide a magnetic field of 8.33 T. The magnets are kept in their superconducting state by cooling them to a temperature of 1.7 K. This is achieved by using cyrogenics, i.e. super-fluid helium. As well as the center of mass energy,
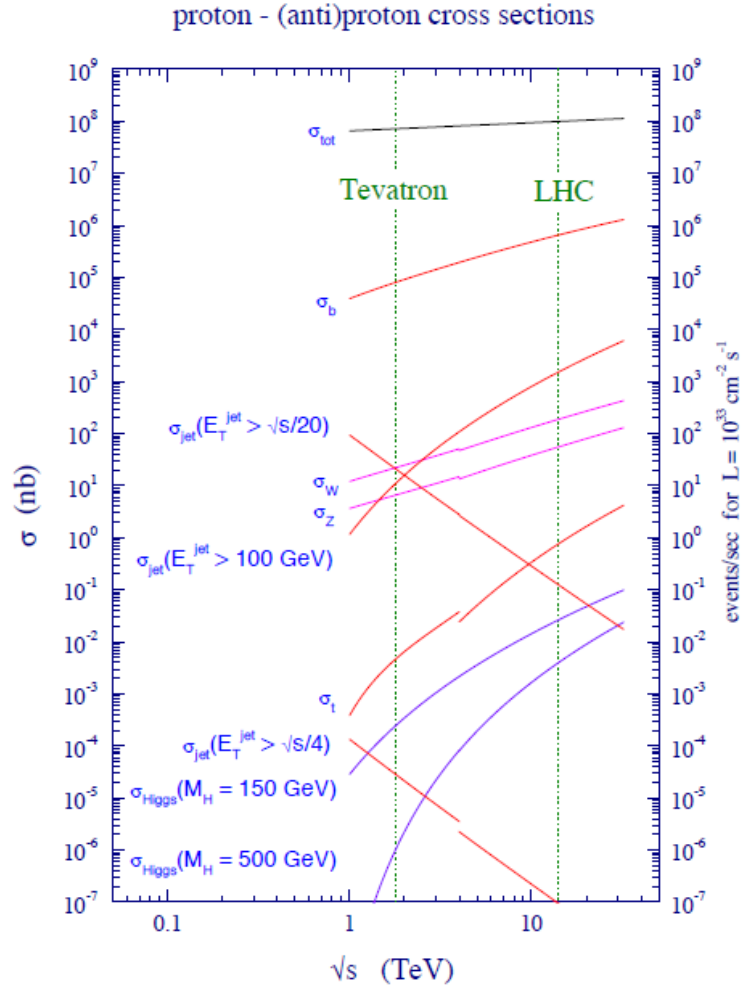
Figure 2.2: Standard Model cross sections at the Tevatron and LHC colliders. [16]

a high event rate is also a crucial parameter to shed light onto new physics at the LHC. The event rate, also known as collision or reaction rate, is given by

$$\frac{dN}{dt} = \sigma L,$$

where σ is the interaction cross section and L is the luminosity. For two oppositely directed beams of relativistic particles the formula for L is

$$L = fn\frac{N_1 N_2}{A},$$

where N_1 and N_2 are the number of particles in each bunch, n is the number of bunches in each beam around the ring and A is the cross sectional area of the beams, assuming them to overlap completely. f is the interaction frequency [17]. Figure 2.2 shows the Standard Model cross sections at the Tevatron and the LHC. As can be seen from the figure, the cross sections for the Higgs bosons with a mass of 150 MeV and 500 MeV are many orders of magnitude lower than their background events. Due to this fact, to be able to observe a sufficient number of Higgs bosons,

a huge number of proton collisions has to be produced. The LHC runs with a peak luminosity of 10^{34} cm^{-2} s^{-1}, 2808 bunches per each beam and 10^{11} protons per bunch and nominal bunch spacing of 25 ns. Due to this high frequency of bunch crossing and the large number of protons in each bunch, collisions can occur simultaneously and overlap. This phenomenon is called pile-up.

2.2   The ATLAS Detector

The ATLAS detector [12] is about 44 m long, 25 m in diameter and has a weight of approximately 7000 tons. The detector is nominally backward-forward symmetric with respect to its interaction point and consists of three subparts. The part closest to the interaction point, the Inner Detector (ID), surrounds the beam pipe and is covered with a solenoid magnet providing 2T magnetic field. The second layer is built by the calorimeter which consists of electromagnetic and hadronic parts. The outermost layer which surrounds the calorimeter is the muon spectrometer. A cut-away view of the ATLAS detector is shown in Figure 2.3.

2.2.1   The ATLAS Detector Coordinate System

In the ATLAS detector, the point where the protons interact, is defined as the origin of the ATLAS detector coordinate system. The beam direction defines the z-axis. The positive x-axis is defined as the direction from the interaction point towards the center of the ring and the positive y-axis points upwards. Because of its transversality to the z-axis, the x-y plane, on which many observables are defined, is called transverse plane and it gives names to the observables such as transverse momentum p_T, transverse energy E_T and missing transverse energy $\not{E}_T$. The azimuthal angle ϕ is measured around the beam axis. The polar angle θ is the angle from the beam axis which defines the pseudorapidity:

$$\eta = -ln\left(tan\frac{\theta}{2}\right). \tag{2.1}$$

And distances in the η-ϕ space are defined as:

$$\Delta R = \sqrt{\Delta\eta^2 + \Delta\phi^2}. \tag{2.2}$$

2.2.2   The Inner Detector

The Inner Detector (ID) [12,18], which is the innermost part of the ATLAS Detector, consists of three sub-detector systems and provides an excellent momentum and vertex resolution as well as fine detector granularity within the region of $|\eta| <$ 2.5. The two high-resolution sub-detectors, the Pixel Detector and Semiconductor Tracker, at inner radii and the Transition Radiation Tracker at outer radii offer these
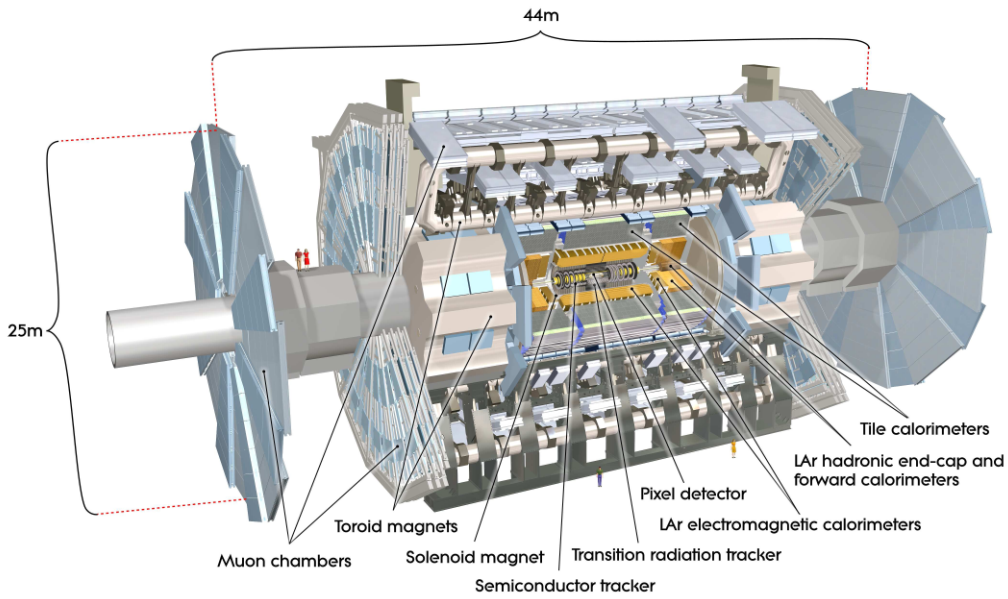
Figure 2.3: ATLAS Detector Layout. [12]

features. The Inner Detector surrounds the beam pipe and extends to a radius of 115 cm and has a length of 7 m, ended by the end-cap calorimetry. A schematic view of the ID is illustrated in Figure 2.4.

The Pixel Detector

The Pixel Detector[12, 18, 19] is designed to detect the tracks of charged particles precisely and it has the most important role for vertex reconstruction, since it is the innermost component. It has three layers in the barrel region at radii $\sim$5 cm, 9 cm, 12 cm and three disks on the transverse plane in each end-cap region at radii between 9 cm and 15 cm.

The main electronic components are 1744 identical modules of which 1456 are in the barrel region and the remaining 288 are in the end-cap region. All of these modules correspond in total to $8{\cdot}10^7$ pixels and cover an area of 1.7 m^2. The modules have an overlapping structure to provide a hermetic coverage. A pixel module is made of a silicon sensor, 21.4$\times$62.4 mm^2 in size, which is subdivided into 46080 pixels with minimum size in $R{-}\phi{\times}z$ of 50$\times$400 μm^2. The intrinsic accuracies are 10 μm ($R{-}\phi$) and 115 μm (z) for both the barrel and end-cap region modules. With these features, the pixel detector provides a very high granularity, precise vertex resolution and the ability to detect short lived particles like b-quarks and τ-leptons.

The Semiconductor Tracker

The purpose of the semiconductor tracker (SCT) [12, 18] is the tracking continuity of charged particles at intermediate radial range of the ID. The SCT has a operating
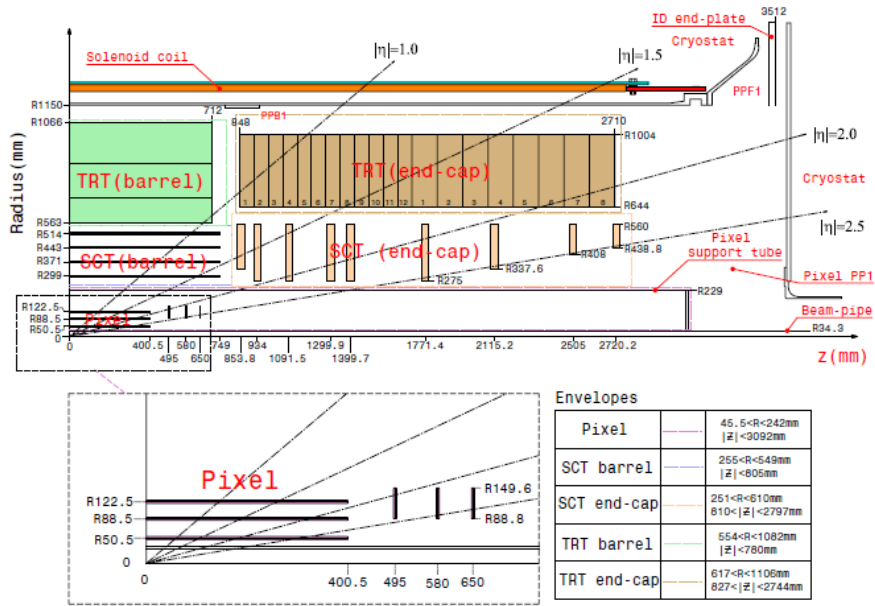
Figure 2.4: Plan view of a quarter-section of the ATLAS inner detector showing each of the major detector elements with its active dimensions and envelopes. The labels PP1, PPB1 and PPF1 indicate the patch-panels for the ID services. [12]

concept similar to the pixel detector, except operating with microstrips instead of pixels.

The SCT comprises four barrel layers between radii 30.0 cm and ∼52.0 cm and nine disks on each end-cap regions between radii 27.5 cm and 56.0 cm. In the barrel region are 2112 modules while 1976 of them are on the end-cap disks. All cover an area of 61.2 m^2 and contain $6.2 \cdot 10^6$ read-out channels.

Silicon modules have a size of 6.36×6.40 cm^2 consisting of 4 microstrip sensors with ∼780 read-out strips and each strip has a 80 μm pitch. In order to provide a two dimensional track reconstruction, these microstrip sensors are glued back-to-back at a 40 mrad angle.

The spatial resolution of the SCT system is 17 μm $(R - \phi)$ and 580 μm (z) both in the barrel and the end-cap region. With the intrinsic accuracies, the SCT has a capability to distinguish two tracks if they are separated by more than 200 μm.

The Transition Radiation Tracker

The outermost component of the ID, the transition radiation tracker (TRT)[12, 18], has a different operating concept from the other two components of the ID. The TRT operates with gas filled straw tubes within the region of $|\eta| < 2.0$.

The TRT comprises 50000 straws, each divided into two halves at the center and 320000 radial straws in the end-cap region. Each straw is 4 mm in diameter and has gold-plated wire with a diameter of 30 μm strained through it. Straws are arranged

parallelly to the beam pipe in the barrel region and have a maximum length of 144 cm, while in the end-cap region, they are 37 cm in length and arranged radially in wheels. They are filled with a non-flammable gas mixture of 70% Xe, 27% CO_2 and 3% O_2. By the use of two independent thresholds in each straw, the TRT is able to distinguish between electrons and pions due to their number of track hits, since ultra relativistic particles, e.g. electrons, produce transition radiations. Therefore, the straws are interlaced with polypropylene fibres in the barrel region and with foils in the end-cap region to be used as transition radiation material. With its 351000 read-out channels, the TRT provides a spatial resolution of 130 μm in $(R-\phi)$. Also, with 36 hits per track, the TRT contributes to the momentum measurement.

2.2.3   Calorimetry

The calorimeters of the ATLAS detector [12], illustrated in Figure 2.5, are sampling calorimeters with a pseudo-rapidity cover range of $|\eta|<4.9$. They are suited for widely varying requirements of the physics processes.The electromagnetic (EM) calorimeter has a fine granularity (typically $\Delta\eta\cdot\Delta\phi\approx 0.025\cdot0.025$) over the η range which is also covered by the ID. The EM calorimeter is well suited for precise measurements of the energies of electrons, positrons and photons. As the outer layer of the ATLAS calorimeter, the hadronic calorimeter (HCAL) has coarser granularity $\Delta\eta\cdot\Delta\phi\approx$ 0.1·0.1, which is sufficient to satisfy the physics requirements for jet reconstruction (See Section 5.1.1) and $\not{E}_T$ measurement. The total thickness of the EM calorimeter is more than 22 and 24 radiation lengths (X_0) in the barrel and end-cap regions, respectively. The thickness of more than 9.7 and 10.0 interaction lengths in the barrel and end-cap regions of HCAL is adequate to provide a good resolution for high energy jets. Measurement of $\not{E}_T$ is important for many physics signatures and is ensured by the large η range and the thickness.

The LAr Electromagnetic Calorimeter

The liquid-argon (LAr) electromagnetic calorimeter[12, 20] comprises a barrel component covering the region up to $|\eta|$=1.475 and two end-cap components 1.375 $< |\eta|$ < 3.2. In the barrel region, the LAr calorimeter is separated into two identical half barrels with a small gap of 4 mm at z=0. The end-cap calorimeters on each side are subdivided into two coaxial wheels. The outer wheel covers the region 1.375 $< |\eta|$ < 2.5 and the inner wheel covers the region 2.5 $< |\eta| < 3.2$. The EM calorimeter is a lead-LAr detector with accordion-shaped polyimide electrodes. It has lead absorber plates over its whole volume. The accordion-shaped design provides complete ϕ symmetry without azimuthal cracks. Within the region up to $|\eta|$=1.8, a presampler detector is used for the correction of the energy which is lost by electrons and photons upstream of the calorimeter.
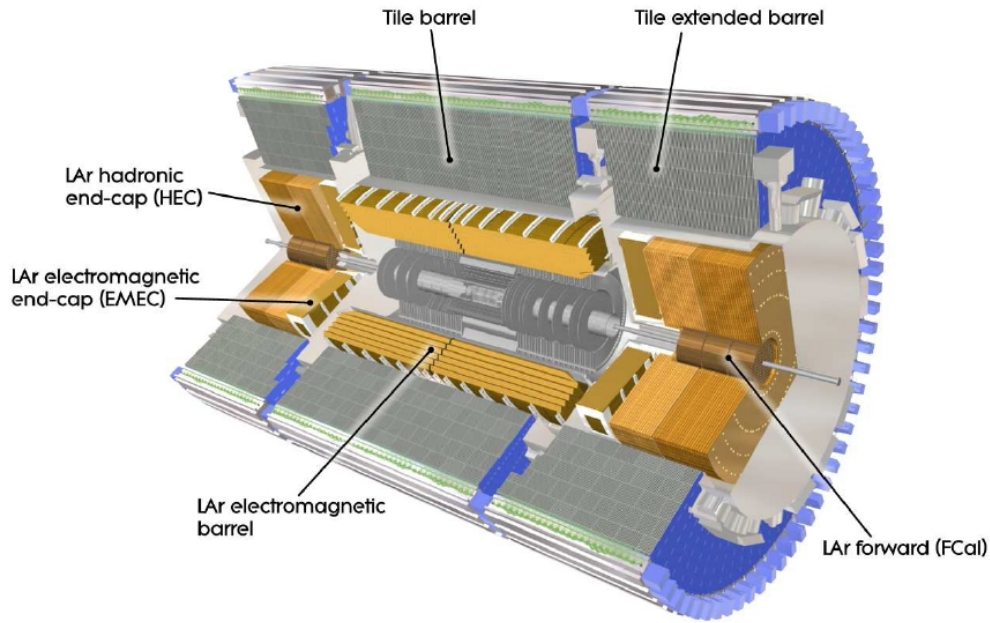
Figure 2.5: Cut-away view of the ATLAS calorimeter system. [12]

Hadronic Calorimeters

The hadronic calorimeter[12] consists of a tile calorimeter, an end-cap calorimeter (HEC) and a forward calorimeter (FCal).

The barrel tile calorimeter and its two extended barrels in the end-cap region, cover a range of $|\eta|<$ 1.0 and $0.8 < |\eta| < 1.7$, respectively. The tile calorimeters are located just behind the LAr EM calorimeter. It is equipped with scintillating tiles as the active medium and with steel as the absorber. Each of the extended barrels as well as the central barrel has a inner radius of 2.28 m and outer radius of 4.25 m. It is segmented in depth in three layers, approximately 1.5, 4.1, 1.8 interaction lengths thick for the barrel and 1.5, 2.6, 3.3 interaction lengths for the extended barrels. The scintillating tiles are read out via two wavelength shifting fibres connected to two separate photomultiplier tubes, which are pseudo-projective towards the interaction region.

The HEC is a sampling calorimeter featuring copper/liquid-argon with flat-plate design covering the range $1.5 < |\eta| < 3.2$. It comprises two independent wheels per end-cap and is located just behind the end-cap EM calorimeter sharing the same LAr cryostats. Each wheel is made of 32 identical wedge-shaped modules assembled with fixtures at the periphery and at the central bore. End-cap wheels are made of copper plates which are interleaved with 8.5 mm LAr filled gaps. Those gaps provide the active medium for the calorimeter.

In order to have the advantage of uniformity of the calorimetric coverage as well as reduced radiation background levels in the muon spectrometer, the FCal is located in the end-cap cryostats. To avoid a high amount of neutron albedo in the
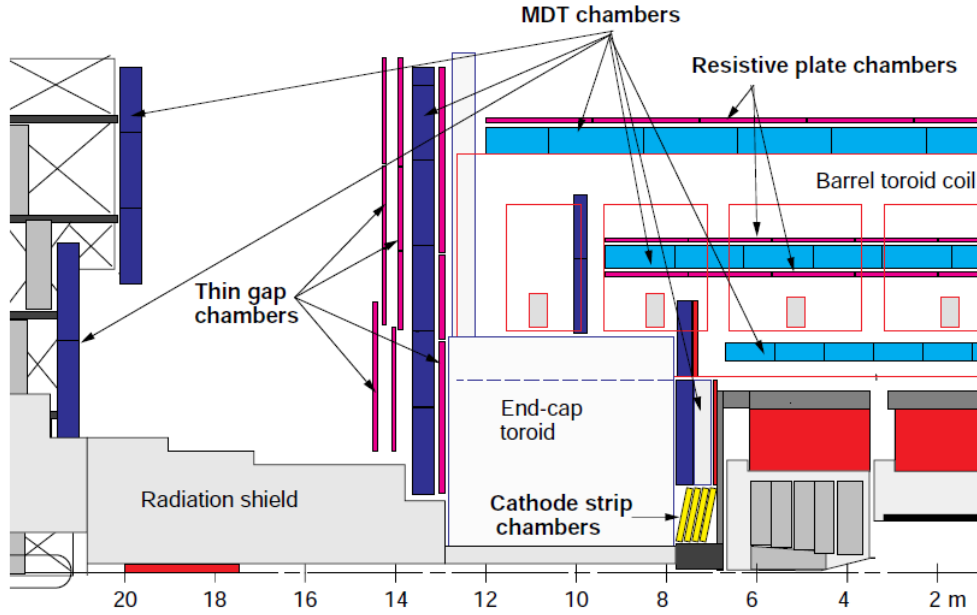
Figure 2.6: View of the ATLAS muon spectrometer. [22]

ID cavity, the front face of FCal is recessed with respect to the EM calorimeter front face and as a consequence of this recess the depth of the FCal is limited. Because of this limitation, the FCal is designed to have high-density. The FCal consists of three modules in each end-cap. The copper module is optimized for electromagnetic measurements and the others, which are both made of tungsten, measure predominantly the energy of hadronic interactions. Each module consists of a metal matrix, with regularly spaced longitudinal channels filled with concentric rods and tubes parallel to the beam axis. The LAr in the gap between the rod and the tube provides the sensitive medium and it has a long term stability.

2.2.4 Muon Spectrometer

The muon spectrometer[12, 21] is the outermost part of the ATLAS detector, since muons are the only charged particles that can penetrate the calorimeter system. Muons with high transverse momenta are often evidence of interesting physical phenomena, such as $Z \rightarrow \mu\mu$ or $H \rightarrow ZZ^{(*)} \rightarrow 4\mu$. The muon spectrometer of ATLAS is able to detect muons in a range up to $|\eta|$=2.7. The spectrometer is also able to trigger on muons in the region $|\eta|$<2.4. The spectrometer is based on the magnetic deflection of muon tracks in the magnetic field generated by three large superconducting air-core toroid magnets. Over the range $|\eta|$<1.4, magnetic bending is provided by the large barrel toroid and for the range between $1.6 < |\eta| < 2.7$, muon tracks are bent by two smaller end-cap magnets which are placed at both ends of the barrel toroid. In the region between the ranges, $1.4 < |\eta| < 1.6$, the deflection is obtained by the combination of barrel and end-cap fields. The spectrometer has

different components. The component, which is responsible for the precision momentum measurement over most of the η region, is the Monitored Drift Tube Chambers (MDTs). MDTs consist of three to eight layers of drift tubes. The tubes are 29.97 mm in diameter, and a tungsten-rhenium alloy wire, 50 μm in diameter, is placed through the tubes as the anode having a potential of 3080 V. By collecting the electrons produced by ionisation at these wires, the MDTs can provide a resolution of 80 μm per tube and 35 μm per chamber. The tubes are filled with a gas mixture of 93% Ar, 7% CO_2 and a small amount ($\leq$1000 ppm) of H_2O. The tubes have an operating gas pressure of 3 bar.

Considering their high spatial, time and double track resolution, Cathode Strip Chambers (CSC) are a good choice to be used in the innermost tracking layer of the muon system. The CSCs are multiwire chambers with cathode planes segmented into strips in orthogonal directions. The system comprises two disks, each has eight small and eight large chambers. By a procedure depending on the signal-to-noise ratio and the read-out pitch of 5.31 mm and 5.56 mm for the large and the small chambers respectively, the CSC reaches a resolution of 60 μm per CSC plane, while the resolution is 5 mm in the non-bending region. CSCs are filled with a gas mixture of 80% Ar, 20% CO_2 and have an operating voltage of 1900 V.

A crucial necessity for the design of the muon spectrometer was the capability to trigger on muon tracks. Therefore, the precision tracking chambers are complemented by a system of fast trigger chambers. These chambers are capable of delivering track information within a few tenths of nanoseconds after the passage of the particle. For this purpose, Resistive Plate Chambers (RPC) in the barrel region, $|\eta| < 1.05$, and Thin Gap Chambers (TGC) in the end-cap region, $1.05 < |\eta| < 2.4$ are used. The RPC is a gaseous parallel electrode-plate detector, which means no wire is used. Two resistive phenotic-melaminic plastic laminate plates are kept parallel to each other at a distance of 2 mm by insulating spacers. The plates have a working electric field of $\sim$5.0 kV/mm between them. This allows avalanches to form along the ionising tracks towards the anode. The RPC uses a gas mixture of 94.7% $C_2H_2F_4$, 5% Iso-C_4H_{10}, 0.3% SF_6. The signals are read out using capacitive coupling to metallic strips, which are mounted on the outer faces of the plates.

Thin Gap Chambers are multi-wire proportional chambers which have smaller wire-to-cathode distance of 1.4 mm than the wire-to-wire distance of 1.8 mm. Within the end-cap region with a highly quenching gas mixture of CO_2 and n-C_2H_5, this cell geometry provides a quasi-saturated mode operation. By the use of high electric field around the TGC, which is $\sim$2900 V, and the small wire-to-wire distance, a very good resolution for a large majority of the tracks is obtained.
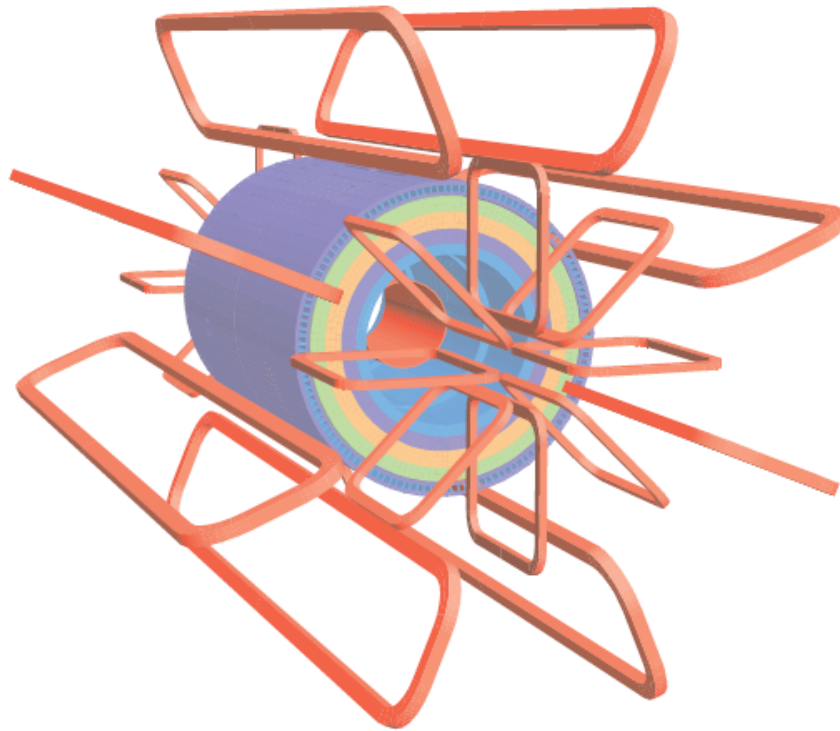
Figure 2.7: Geometrical view of the ATLAS magnet system. [12]

2.2.5   The Magnet System

The magnet system of the ATLAS detector[12] plays a crucial role for the measurement of charged particles momenta. The tracks of charged particles are bent in the magnetic field, provided by a system of superconducting magnets.

The solenoid magnet, as mentioned in Chapter 2.2, surrounds the ID and provides a homogeneous axial magnetic field of 2 T at an operating temperature of 4.5 K. Since the solenoid magnet is located in front of the EM calorimeter, minimisation of the material-density is important to achieve the desired measurement performance in the EM calorimeter. Due to this, the solenoid magnet and LAr calorimeter share the same vacuum vessel.

The second magnet system, a barrel toroid and two end-cap toroids produce magnetic fields of 0.5 T and 1.0 T, respectively. Each toroid comprises eight air-core superconducting coils. In the barrel toroid each coil has its own cryostat, while each end-cap toroid has a general cryostat. The toroid magnet system provides the magnetic field for the muon spectrometer.

2.2.6   The Trigger System

Due to the high interaction rate, $\sim$1 GHz, a sophisticated trigger system[12] is needed for the reduction of the amount of data which is going to be recorded and analysed. Therefore, a trigger system is implemented, which can reduce the data
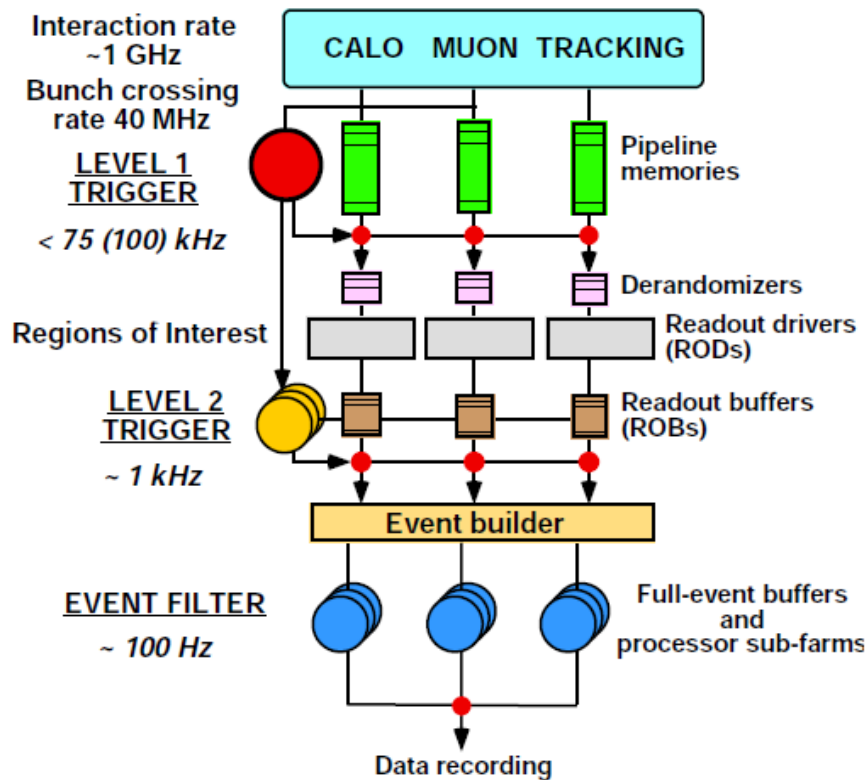
Figure 2.8: Block diagram of the ATLAS trigger and data acquisition systems. [23]

bunch crossing rate from 40 MHz down to data taking rate which is approximately 100 Hz. The trigger system is structured in three levels.

The task of the first level trigger, L1, is to search for high transverse-momentum muons, electrons, photons, jets and τ-leptons decaying into hadrons as well as large missing and total transverse energy. The selection of L1 is based on information obtained by detector subsets. Identification of high transverse-momentum muons is performed by the RPCs and TGCs of the muon spectrometer. Another feature of the L1 trigger is to define one or more Regions-of-Interest (RoI) for each event. RoIs are the geographical coordinates in η and ϕ of those regions within the detector where its selection process has identified interesting features.

The L2 selection uses the information provided by the RoI by the L1 trigger. All available data within the RoIs, at full granularity and precision, which is approximately 2% of the total data, is used by the L2 selection. L2 menus are able to reduce the trigger rate down to approximately 3.5 kHz.

At the last step of the trigger system, the event filter (EF) reduces the event rate down to its final level, which is roughly 100 Hz. Selections of the EF are implemented using offline analysis procedures within an average event processing time of the order of four seconds.

Chapter 3

Top Quark Physics at the LHC

The observation of the top quark [24, 25], in 1995 by the CDF and DØ experiments at the TEVATRON accelerator at the FERMILAB, was a crucial achievement on the way of completing the missing pieces of a nice 'puzzle', the Standard Model. Although the top quark was theoretically hypothesized with its weak-isospin partner, the bottom quark, in 1973 by Kobayashi and Maskawa [3], it could only be observed a long time after the bottom quark because of its huge mass, which was not able to be produced until an accelerator powerful enough was built.

The top quark with its weak-isospin partner, the bottom quark, completes the third generation. Due to the large mass of the top quark being by far the heaviest of all quarks, it is often speculated that it might be special amongst all quarks and leptons and might play a role in the mechanism of electroweak symmetry breaking.

3.1   The Standard Model of Particle Physics

Quantum field theory (QFT) is a combination of two great achievements of physics, quantum mechanics and relativity [26]. The standard model of particle physics is a particular quantum field theory. The current form of its formulation was concluded in the middle of the 1970s with the confirmation of quark existence and since then the theory has stood up many experimental tests. It describes elementary particles, of which the universe is made up, and the interactions of these particles with each other. The visible matter of the universe is made up of fermions, spin 1/2 particles. These particles interact with each other due to the exchange of particles called gauge bosons, spin 1 particles. The standard model states that the matter is constituted from twelve fermions and their anti-particles. The existence of an anti-particle for each charged massive fermion is correctly predicted by the Dirac equation. According to this equation the anti-particles have the same mass and spin but opposite charge and magnetic moment relative to the direction of spin [28].

Fermions are separated into six leptons and six quarks. The leptons are classified in three families, each with two family members, electron, muon, tau and their

**Three Generations
of Matter (Fermions)**

I	II	III	

| mass→ 2.4 MeV
charge→ ⅔
spin→ ½
name→ **u**
up | 1.27 GeV
⅔
½
c
charm | 171.2 GeV
⅔
½
t
top | 0
0
1 **γ**
photon |

Figure 3.1: Elementary particles of the standard model [27]

corresponding neutrinos, which are neutral leptons, as the second member of each family. The second and the third generation charged leptons, muon and tau, are just heavier forms of the electron and due to their unstable character, they spontaneously decay to electrons, neutrinos and other particles [17].

Like leptons, quarks are classified in three families, each with two members but unlike leptons, all quarks carry non-integer electric charge, being $+2/3$ e or $-1/3$ e. The quark families are formed by three weak-isospin doublets which consists of up(u) and down(d), charm(c) and strange(s), top(t) and bottom(b), respectively.

Finally, gauge bosons are mediator particles which mediate the interactions between the fermions described above. The bosons also have integer electric charge. There are particular bosons for different types of interactions and those are W, Z bosons, photon and gluon. The only particle in the standard model which is not observed yet is the Higgs Boson. Theoretical existence of the Higgs boson is described by the Higgs mechanism [1,2]. As mentioned in the first chapter, the search for Higgs is one of the main focus points at the LHC.

3.1.1   Fundamental Forces

Four types of interactions rule the universe. Gravitational, strong, electromagnetic and weak force. All types of particles are subject to the gravitational force. However, on the scale of particle physics experiments, gravity is by far the weakest of all fundamental forces, although it is dominant on the scale of universe. The other interactions are mathematically represented with the principle of local gauge invariance and the symmetry group $SU(3)_C \bigotimes SU(2)_L \bigotimes U(1)_Y$, where $SU(3)_C$ is the group of QCD and $SU(2)_L \bigotimes U(1)_Y$ is the symmetry of electroweak interactions which is unification of electromagnetic and weak interaction. An illustration of interactions between Standard Model particles is shown in Figure 3.2.
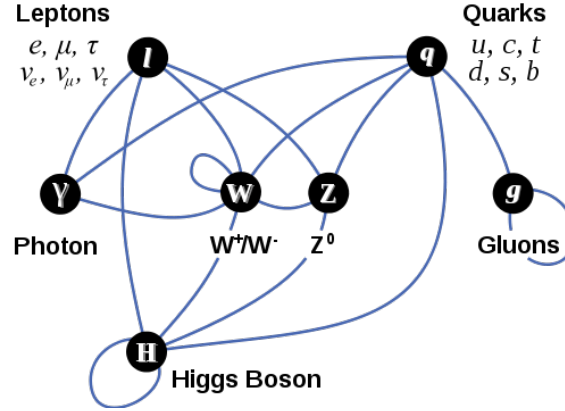
Figure 3.2: Interactions of the standard model [27]

The Strong Force

The quantum field theory of the strong force is QCD and its gauge symmetry group is $SU(3)_C$ which is, in contrast to QED, a non-Abelian group where the subscript C stands for colour charge [29]. 'Colour' is the charge of quarks and gluons which are particles subject to the strong force. Three different colour charges exist; red, green, blue and their 'anti'-charges. As the gluons are mediator particles of the strong force, they carry combinations of these colour charges and with this feature, they can interact with themselves. As a consequence of this interaction, the required energy to separate the quarks is proportional to the distance between them. Due to this fact, the quarks can not exist in nature as free particles. This is referred to as quark confinement. The coupling constant of the strong force is calculated by the following formula [29]:

$$\alpha_s(Q^2) = \frac{12\pi}{(33 - 2n_f)\log(Q^2/\Lambda^2)}. \tag{3.2}$$

where Q^2 is defined as the square of the momentum transfer between gluons in an interaction, n_f is the number of flavours and Λ is the parameter for the QCD scale. At the scale where $Q^2 > \Lambda^2$ the strong coupling is weak and the quarks are quasi-free. For Q^2 of order of Λ^2, the coupling is strong and as a consequence the quarks and gluons are in strongly bounded states, which are called hadrons. In high energy collisions, such as at LHC, the quarks can fly apart for a short moment and once they reach a separation distance of around 1 fm, which is the diameter of a hadron, a new quark-antiquark pair is produced since their interaction is so strong. These quark-antiquark pairs join together and create mesons and baryons. This phenomenon is called hadronisation and is illustrated in Figure 3.3.
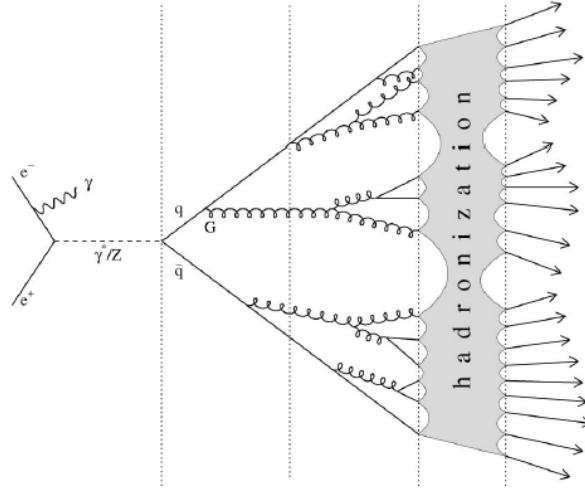
Figure 3.3: Schematic representation of an $e^- - e^+$ annihilation process into hadrons [30].

The Electromagnetic Force

The QFT of the electromagnetic interaction is QED. As mentioned above, the symmetry group of this interaction is $U(1)_Y$, where the subscript Y stands for weak hypercharge. The interaction involves all electrically charged elementary particles and the corresponding gauge boson, photon, as the mediator particle.

Since the photon has no electric charge, it can not couple to itself. The coupling constant for the electromagnetic interaction is given by the following formula [29];

$$\alpha(Q^2) = \frac{\alpha(\mu^2)}{(1 - \frac{\alpha(\mu^2)}{3\pi}) \log(\frac{Q^2}{\mu^2})},$$ (3.3)

where $\alpha(\mu^2)$ is the value of the coupling constant evaluated at the renormalization momentum, μ.

The Weak Force

It is the electric charge that produces the electromagnetic force, and it is the colour charge that produces the strong force. There is no explicit term for the thing that produces the weak force but all leptons and quarks are involved in this force. On the other hand, the quantum number of the interaction is called flavour. The gauge symmetry group of the interaction is $SU(2)_L$ and the mediator particles are $W^\pm$ and Z^0 bosons. In opposition to photon and gluon, $W^\pm$ and Z^0 bosons are massive particles where m_W=80.399±0.023 GeV and m_Z=91.1876±0.021 GeV, respectively [31].

Due to the difference of the electric charge of the mediator particles, two kinds of weak interaction exist; the interaction via charged $W^\pm$ bosons, which is called charged weak current and the interaction via Z^0 boson which is called neutral weak current. Via charged weak current, a charged lepton can absorb a W boson and
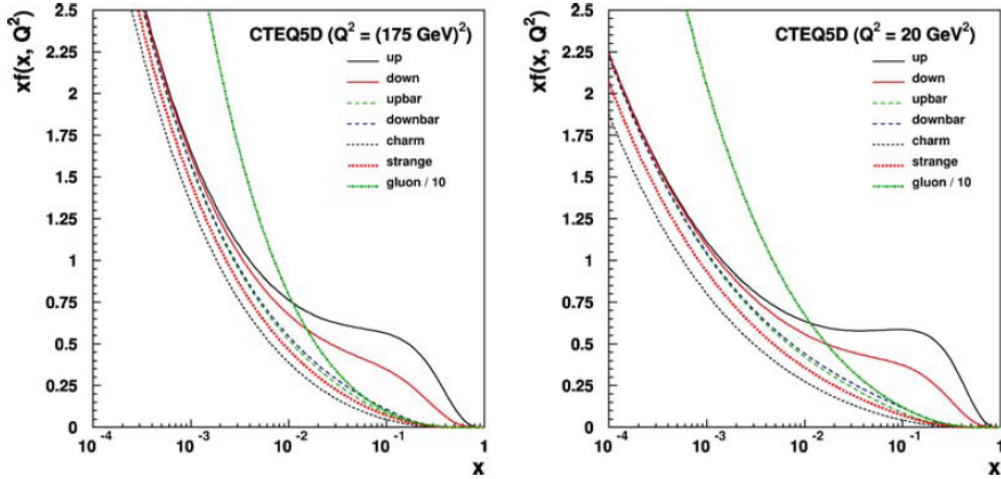
Figure 3.4: The quark, antiquark and gluon momentum densities in the proton as a function of the longitudinal proton momentum fraction x at $Q^2 = m_t^2$ (left) and at $Q^2 = 20 \text{GeV}^2$ (right) from the CTEQ5D parameterisation.[32]

thereby it is converted to corresponding neutrino, which is the other member of the generation. Leptons can also change their flavours via charged weak currents. For example, a muon can decay into an electron and additionally two neutrinos via weak interaction. This is called flavor changing charged current. Similar to this process, quarks can also change their flavour emitting a W^- boson (or absorbing a W^+). Then, the emitted W boson decay immediately. In this case, the information of probability for into which flavour the quarks convert after emitting or absorbing a W boson is provided by the CKM(Cabibbo-Kobayashi-Maskawa) unitary matrix. It can be seen that the probability for a coupling within the same generation is almost one for all three generations.

$$|V_{CKM}| = \begin{bmatrix} |V_{ud}| & |V_{us}| & |V_{ub}| \\ |V_{cd}| & |V_{cs}| & |V_{cb}| \\ |V_{td}| & |V_{ts}| & |V_{tb}| \end{bmatrix} = \begin{bmatrix} 0,9742 & 0,2253 & 0,0034 \\ 0,2252 & 0,9734 & 0,0410 \\ 0,0086 & 0,0403 & 0.9991 \end{bmatrix} \qquad (3.4)$$

3.1.2 Top Quark Production

As mentioned before, the observation of the top quark was not possible before the TEVATRON due to its huge mass. Until the LHC has started to operate, TEVA-TRON was the only accelerator capable of producing top quarks. But, since the TEVATRON has shut down at September 30th 2011 [33], the LHC is the only accelerator where top quark production is possible. At hadron colliders, the top quarks can be produced both in $t\bar{t}$ pairs and as single particles. The latter is not of interest for the topic of this thesis and is therefore not described.

The $t\bar{t}$ pair production is possible via the strong interaction as well as electroweak
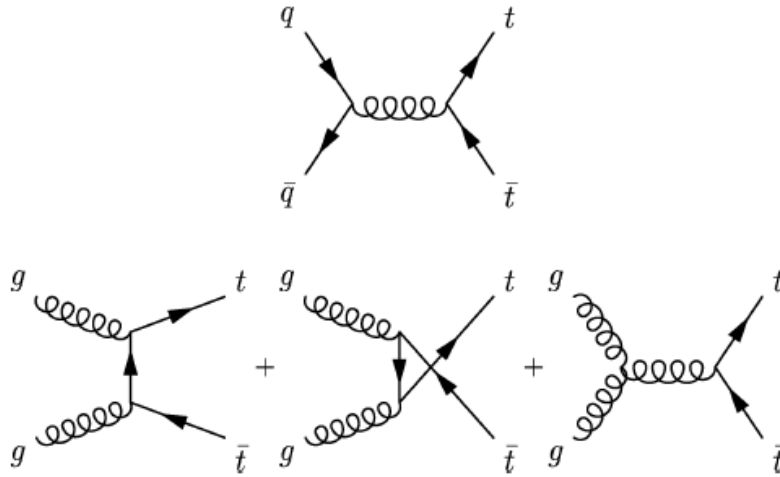
Figure 3.5: Top-quark pair production via the strong interaction at hadron colliders proceeds at lowest order through quark anti-quark annihilation (top) and gluon fusion (bottom). [26]

interaction by exchanging a Z^0 or a photon but the cross section for top pair production via γ/Z^0 is completely negligible at hadron colliders [34]. The $t\bar{t}$ pair production at high energy interactions of a $p\bar{p}$ or a pp collision at the TEVATRON or LHC, respectively, is described by perturbative QCD [26]. In this approach, the constituents (partons) of colliding protons are quarks and gluons. They interact directly with each other. The partons carry varying fractions x of the momenta of their parent hadrons. Hadron collisions can be described both as a short distance (hard scattering) partonic cross section and as a long distance which are factored into the parton longitudinal momentum distribution functions (PDFs) $f_i(x_i, Q^2)$. This separation is called factorization and is set by the energy scale , Q^2. The PDFs, $f_i(x_i,, Q^2)$, can be interpreted as the probability density to observe a parton of flavour i and longitudinal momentum fraction x_i. The PDFs can not be calculated a priori by perturbative QCD, but are measured in experiments. An example parametrisation is illustrated in Figure 3.4. The total cross section for hard scattering processes of a pp or a $p\bar{p}$ collision with a center-of-mass energy $\sqrt{s}$ can be calculated as follows [26]:

$$\sigma^{pp\to t\bar{t}}(\sqrt{s}) = \sum_{i,j=q,\bar{q},g} \int dx_i dx_j f_i(x_i, Q^2) f_j(x_j, Q^2) \cdot \hat{\sigma}^{ij\to t\bar{t}}(\rho, x_i, x_j, Q^2). \quad (3.5)$$

$f_i(x_i, Q^2)$ and $f_j(x_j, Q^2)$ are the PDFs for the proton and (anti)proton, while the summation indices i and j run over all $q\bar{q}$, gg pairs, $\rho=4m_t^2/\sqrt{\hat{s}}$ and $\hat{s}=x_i x_j s$ is the effective center-of-mass energy squared for the partonic process. The corresponding Feynman diagrams of the lowest order $t\bar{t}$ pair production processes are illustrated in Figure 3.5.

Undoubtedly, there has to be at least enough energy to produce a $t\bar{t}$ pair at
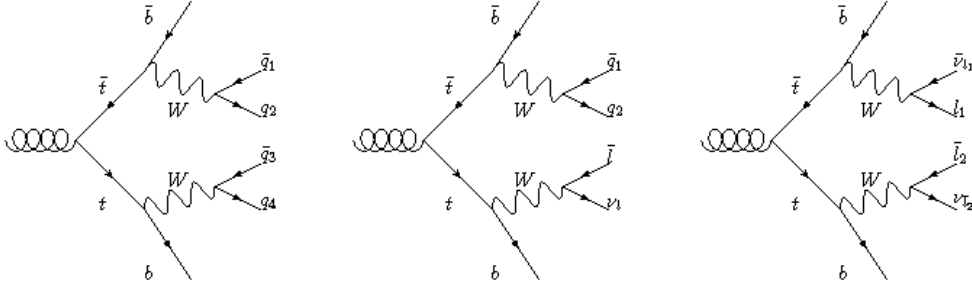
Figure 3.6: Schematic diagrams of the three $t\bar{t}$ decay channels: The alljets channel (left); the lepton+jets channel (middle); the dilepton channel (right). [26]

rest, i.e. $\hat{s} \geq 4m_t^2$. Therefore, $x_i x_j = \hat{s}/s \geq 4m_t^2/s$. With an assumption of setting $x_i \approx x_j \equiv x$, the approximate value of x becomes 0.025 for the LHC. This shows that at the LHC the $t\bar{t}$ pair production is dominated by the gg fusion as can be clearly seen in Figure 3.4.

3.1.3 Top Quark Decay

The top quark has a very unstable character due to its huge mass. As a consequence of this instability the lifetime of the top quark is extremely short, $\tau_t \simeq 1/\Gamma_t \approx 5 \cdot 10^{-25}$ s where the decay width of the top quark, Γ_t, is given by the following formula [26],

$$\Gamma_t = \frac{G_F m_t^3}{8\pi\sqrt{2}} \left(1 - \frac{M_W^2}{m_t^2}\right)^2 \left(1 + 2\frac{M_W^2}{m_t^2}\right) \times \left[1 - \frac{2\alpha_s}{3\pi}\left(\frac{2\pi^2}{3} - \frac{5}{2}\right)\right] \quad (3.6)$$

with the Fermi coupling constant $G_F = 1.16637 \times 10^{-5}$ GeV^{-2}, the W boson mass M_W, and the top mass m_t. Since the lifetime of the top quark is shorter than QCD hadronisation time, i.e., $\tau_{had} \simeq 1/\Lambda_{QCD} \approx 3 \times 10^{-24}$ s, the top quark decays before it forms a bound state. The top quark decays preferentially into a W boson and a b-quark. The b-quark then hadronises, while the W boson decays into lepton or quark pairs. The decay products of the two W bosons classify the decay channels of the top quark pair as follows:

- A. $t\bar{t} \to W^+ b W^- \bar{b} \to q\bar{q}' b q'' \bar{q}''' b$,   (46.2%),
- B. $t\bar{t} \to W^+ b W^- \bar{b} \to q\bar{q}' b l \bar{\nu}_l \bar{b} + \bar{l}\nu_l b q \bar{q}' \bar{b}$, (43.5%),
- C. $t\bar{t} \to W^+ b W^- \bar{b} \to \bar{l}\nu_l b l' \bar{\nu}_{l'} \bar{b}$,   (10.3%).

The first, the second and the final cases refer to the fully-hadronic, the semileptonic and the dileptonic channels, respectively. The W boson can decay into any three generation of lepton pairs and only the first and the second generation of quark pairs, each in three different colour states. The decay channels of top quark are shown in Figure 3.6. Branching ratios of the W boson at Born level with respect to fermion universality in electroweak interactions are represented in Table 3.1 and the
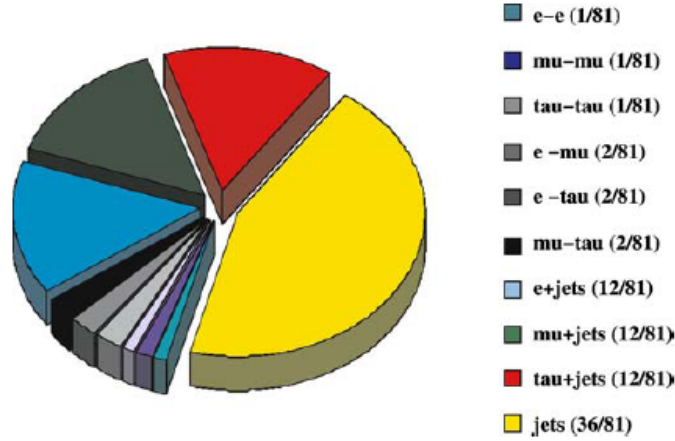
Figure 3.7: Pie chart of the branching ratios of the different $t\bar{t}$ decay channels at Born level.[26]

resulting decay branching ratios for the top quark pair are presented in Figure 3.7.

High QCD background for the fully-hadronic channel at the LHC and low branching ratio for dileptonic channel make the semileptonic channel the favorite channel for top quark analyses.

Table 3.1: The decay channels of the W^+ boson and corresponding branching ratios.

Decay Mode	Branching Ratio
$W^+ \to e^+\nu_e$	10.72±0.16 %
$W^+ \to \mu^+\nu_\mu$	10.57±0.22 %
$W^+ \to \tau^+\nu_\tau$	10.74±0.27 %
$W^+ \to l^+\nu_l$	32.04±0.36 %
$W^+ \to u\bar{d}, c\bar{s}$	67.96±0.35 %

3.1.4 Radiative Top Quark Processes

Radiative top quark processes can be classified in two groups, radiative top quark production and radiative top quark decay [35]:

- $pp \to t\bar{t}\gamma \to l^\pm\nu b\bar{b}jj\gamma$,
- $pp \to t\bar{t} \to b\bar{b}W^+W^-\gamma \to l^\pm\nu b\bar{b}jj\gamma$.

As mentioned in Section 3.1.2, the top quarks are produced either via gluon fusion or quark anti-quark annihilation. In the radiative top quark production via gluon fusion, the photon can only be radiated off one of the top quarks. In the quark anti-quark annihilation, the photon can also be radiated off one of the incoming quarks. In this process, the top quark is assumed as a stable particle, which means
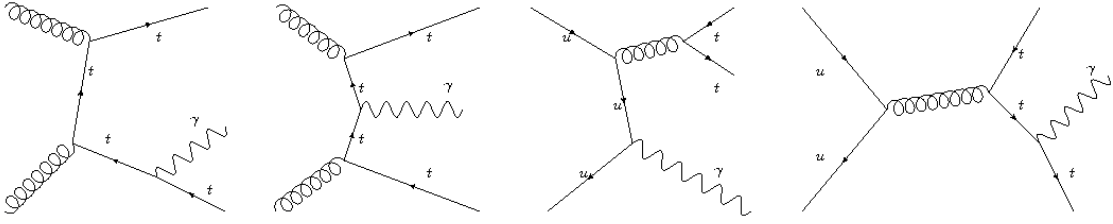
Figure 3.8: The radiative top quark production processes via gluon fusion(first two diagrams) and quark anti-quark annihilation. Via gluon processes the photon is radiated off either the top quark pair or a virtual top quark. In the quark anti-quark annihilation case,the photon is emitted by one of the incoming quarks or by the top quark.
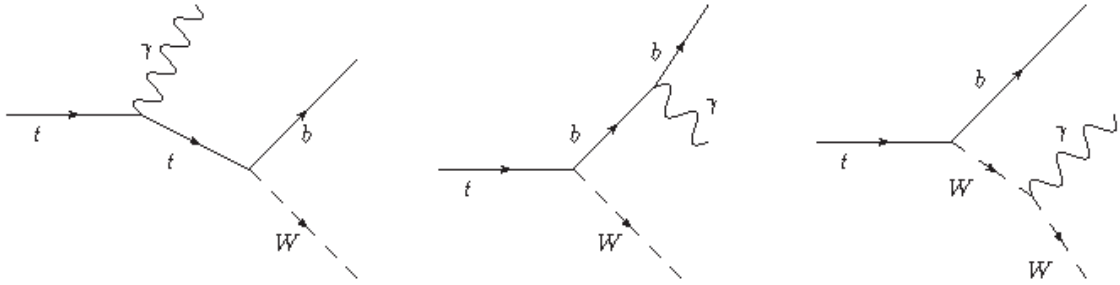
Figure 3.9: The radiative top quark decay processes. The photon can be radiated off the top quark or one of its decay products. Only one top quark is shown.

the photon is radiated off a virtual (off mass shell) top quark. Feynman diagrams for radiative top quark production processes are shown in Figure 3.8 [36].

In the radiative top quark decay, the photon can be emitted by an on mass shell top quark as well as by the bottom quark or W boson from the top quark decay. Only photons radiated off the top quark have importance for the top quark charge measurement. Feynman diagrams for the radiative top quark decay processes are shown in Figure 3.9 [36]. Since the $t\bar{t}$ production is dominated by gluon fusion at the LHC, one expects that the $pp \rightarrow t\bar{t}\gamma$ cross section should be proportional to the charge of the top quark squared, Q^2_{top}.

Experimentally, it is not possible to distinguish between the radiative top quark production and the radiative top quark decay. Only the full event, which is determined by the final state, can be detected.

Chapter 4

Monte Carlo Generators and Detector Simulation

Data simulation is an indispensible tool for today's particle physics. It has great importance in two aspects. First, as the collision energy of experiments goes up higher and higher, events with more and more outgoing particles, with more and more complex structure come up. Therefore, a tool is needed to represent this complexity in enough detail. The other aspect is that data simulation provides an opportunity to predict the requirements of a new detector and to design it as well as to develop and optimize possible analysis strategies. Then, by comparing real and simulated data, the physical models are confirmed or refused at a certain confidence level. The essential component of the data simulation are the event generators. This chapter discusses the basic processes of a hadron-hadron collision simulated in event generators as well as the detector simulation process which comes after the event generation stage.

4.1   Event Generation with Monte Carlo Generators

Basically, an event generator simulates events mimicking the real physical interactions in the particle collisions. They use random numbers and a given theoretical model for event simulation. At the end of the simulation process, an output is obtained as the same output of the real collisions in the particle detectors. However, the simulation process is not so easy. Therefore, the whole process is decomposed and handled separately. Considering a high energy hadron-hadron collision, an event generator should implement the following steps: two initial beam particles characterized with parton distribution functions, hard scattering process, initial and final state radiation, hadronisation of outgoing quarks and gluons, decay of unstable produced hadrons and multiple interactions. A schematic illustration of a hadron-hadron collision can be seen in Figure 4.1.
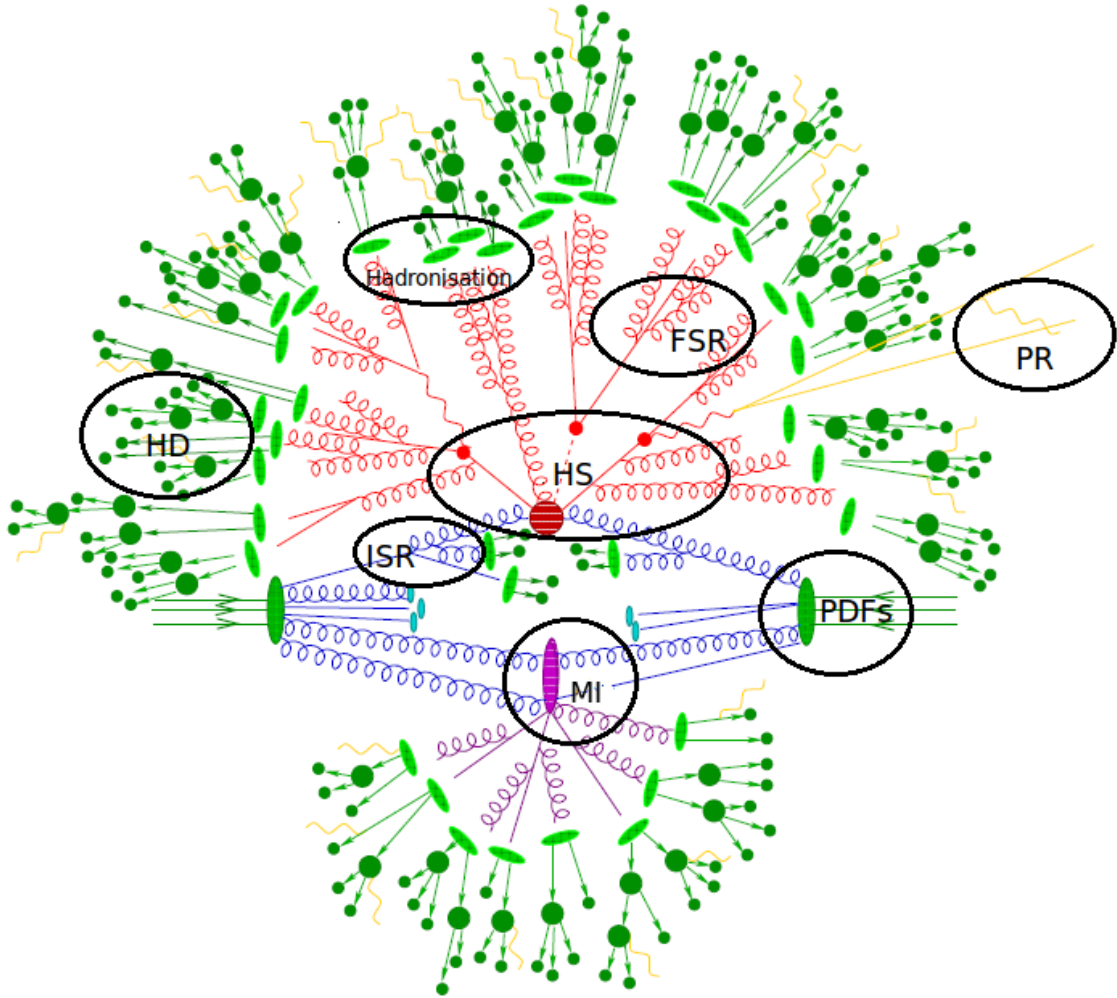
Figure 4.1: Illustration of typical hadron-hadron collision. A hard scattering(HS) occurs between the partons of incoming protons described by parton distribution functions(PDFs). Gluons are radiated off the incoming parton(ISR) as well as an additional hard QCD radiation from outgoing particles(FSR). A secondary interaction takes place as multiple interaction(MI) before the final-state partons hadronise (Hadronisation) and hadrons decay(HD). Photon radiation occurs at any stage(PR) [37].

4.1.1 Hard Scattering Process

The hard scattering process is the essential process in the hard collision. The interaction of incoming partons and production of new particles are described by the hard scattering process. Due to the description of the QCD factorization theorem (See Section 3.1.2), hard collisions are separated into short and long distance interactions. Hard scattering, as a short distance interaction, occurs at large energy scale Q^2 where the coupling constant $\alpha_s(Q^2)$ is much smaller than one. Therefore matrix elements (ME) can be calculated perturbatively. This is done by ME generators. As the energy scale approaches to zero, the strong force becomes stronger. This is the region where QCD confinement works and perturbative QCD is not valid at all.
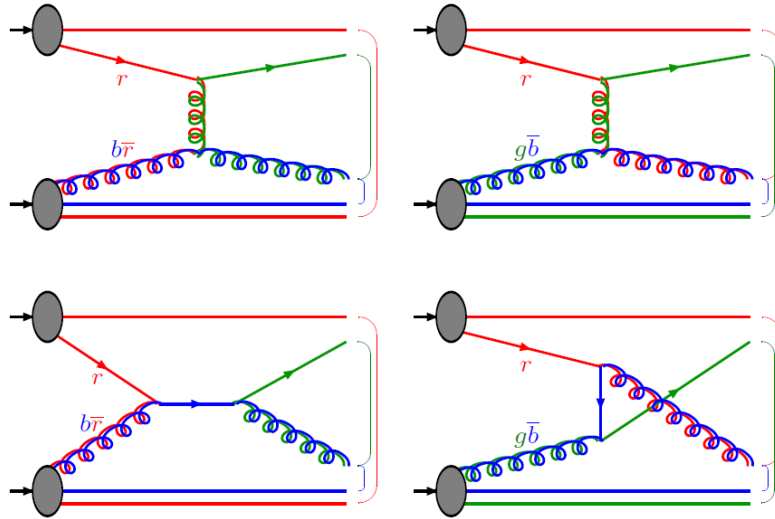
Figure 4.2: Possible colour flow configurations of outgoing partons [16].

Colour Flow in Hard Scattering Processes

Colour flow is a significant issue, which must be considered in the generation of the hard scattering processes. Quarks carry colour charge and gluons carry colour charge combination. Because of this, different possibilities for colour combination of outgoing partons are possible. Therefore, a colour flow configuration has to be done just before the hadronisation process. The configuration is needed for the upcoming steps of event generation such as: hadronisation and showering processes. Different parton shower algorithms handle this issue in different ways. Some examples of colour flow configurations can be seen in Figure 4.2.

4.1.2   Initial and Final State Radiation

In hard scattering processes of hadrons, incoming and outgoing partons are colour charged particles and they radiate gluons. These gluon radiations generate 2→3, 2→4 (and so on) final states starting from a basic 2→2 process. Since these radiations are important for jet production in events, they have to be handled in the event generation process and there are two ways to handle these radiations.

The first way to handle these radiations is the matrix element method. In this method, Feynman diagrams are calculated order by order. However, there are disadvantages of this method. One of the disadvantages is that emission of soft gluons ($E_g \downarrow 0$) and collinear gluons ($\theta_{qg} \downarrow 0$) cause two divergences in the calculation. The other disadvantage is that the calculations become more and more complex at higher orders [38].

The second way, which is often preferred due to its simplicity and flexibility, is the parton shower approach. With this approach, the hard scattering process is calculated separately and then the incoming and the outgoing partons are dressed up with
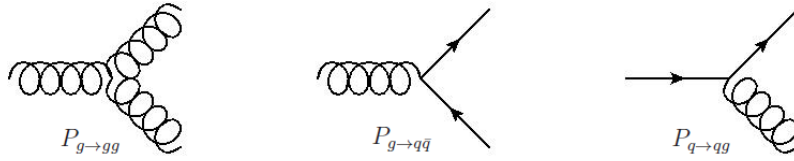
Figure 4.3: Feynman Diagrams of DGLAP Splitting Kernels

parton showers. In the shower approach, the kinematics of radiations (branchings) is described in terms of two variables, Q^2 and z. Various parton shower programs differ from each other on the interpretation of these variables. Q^2, the evolution variable, is related to either the mass or transverse momentum or opening-angle scale of the branching and it has the dimension of squared mass. The other variable, z, is defined as the momentum fraction of one of the daughter parton, while the other daughter carries $(1 - z)$ of the momentum. The branching can be considered as $a \to bc$, where a is the 'mother', while b and c are the daughter partons. Besides the evolution variable and momentum fraction, the branching is performed using evolution equations (also called DGLAP splitting functions) and Sudakov form factor [39]. DGLAP (Dokshitzer-Gribov-Lipatov-Altarelli-Parisi) splitting functions give the probability for a parton to branch, while the Sudakov form factor gives the probability of not having a parton branching in a specified interval. Details can be found for DGLAP splitting functions in [40–43] and for Sudakov form factor in [44]. Feynman diagrams of QCD DGLAP splitting kernels are shown in Figure 4.3. For the parton shower approach, PYTHIA and Herwig are two general purpose programs having different properties. They are widely used in the ATLAS Collaboration. In the event generation, they are responsible for the hard scattering, initial and final state radiations as well as hadronization and decay processes of outgoing quarks.

Final-State Radiation

Final-state radiations (FSR) are timelike, which means partons have $m^2 = E^2 - \mathbf{p}^2 \geq 0$. Therefore, the evolution variable Q^2 has been defined as the squared mass of the branching parton in PYTHIA [39, 45]. However, the current definition in PYTHIA is p_T-ordered, i.e. $Q^2 = p_T^2 = z(1 - z)m^2$. On the other hand, Herwig uses angular ordering, $Q^2 = E^2(1 - cos\theta) \approx m^2/(z(1 - z))$, where the θ is the angle between the mother and daughter partons. The strategy for the final-state radiation is that starting from a maximum scale Q^2_{max}, an original parton is evolved downwards in Q^2 until the branching occurs. The selected Q^2 value now is the p_T (in PYTHIA) or emission angle (in Herwig) of the new parton b.

Initial-State Radiation

In opposition to final-state radiation, initial-state radiations (ISR) are spacelike i.e. off the mass shell. This means, in the branching sequence $a \rightarrow bc$, the partons a and b have $m^2 = E^2 - \mathbf{p}^2 < 0$. The other daughter parton, which is not involved in hard scattering, may have timelike virtuality. Unlike FSR, the evolution of ISR is characterised by the evolution variable $Q^2 = -m^2$. The theoretical analysis of ISR is more complex than that of FSR. The handling of ISR is backwards due to evolution variable Q^2. By this way, the choice of the hard scattering is based on the use of evolved parton distributions, in which the effects of initial state radiations are already included.

4.1.3   Hadronisation and Decay of Hadrons

Hadronization (also called fragmentation) is a process valid at long distances where the perturbative QCD breaks down. The hadronisation process describes how hadrons are formed from quarks and gluons after parton showering. After the formation of hadrons, the unstable ones decay into stable particles which can be observed in the detector.

There are two fragmentation models which are described below. The former is used by PYTHIA and the latter by Herwig.

String Fragmentation

The understanding of string fragmentation is based on a linear confinement picture [39], in which the energy stored in the colour dipole field between a charge and an anticharge increases linearly. This picture provides the original point for a model called string model. Due to this, as the quark and antiquark partons move apart from each other, a colour flux tube is stretched between the quark and antiquark. The energy stored on the string is proportional to the distance between the quarks. When the energy of the string reaches a certain level, the string breaks down due to the production of a new quark-antiquark pair. If the invariant mass of either of these string pieces is large enough, further breaks may occur. Hadrons are then formed from these partons.

Cluster Fragmentation

Cluster fragmentation model basically rely on preconfinement property of perturbative QCD [46]. The preconfinement is the clustering of colour-anticolour quark pairs which decay later on into the observed hadrons.

Outgoing gluons split non-perturbatively into quark-antiquark or diquark anti-diquark pairs after the perturbative parton shower. Each jet at this point consists of outgoing quarks and antiquarks. By neighbouring quark-antiquark pairs, colour

singlet clusters are formed which are later fragmented into hadrons. If a cluster is not massive enough to decay into two hadrons, it is taken simply to present the lightest single hadron of its flavour.

Decay of Hadrons

Most of the hadrons produced at the end of the fragmentation processes are unstable and they decay into the observable stable particles. Therefore, it is important to include all particles with their mass distributions and decay properties. These informations are obtained by experimental data and the decay process is performed according to these informations [39].

4.1.4   Multiple Interactions

As a consequence of the composite structure of protons, besides the partons involved in the hard scattering, other partons also interact. These interactions are named multiple interactions. Since the multiple interactions occur mainly at low p_T, they are soft interactions compared to the hard scattering. But they contribute to the total multiplicity in the event.

For the handling of multiple interactions, PYTHIA has its own model, while Herwig uses an external model, called JIMMY [47]. PYTHIA's model is more complex compared to JIMMY. PYTHIA provides a description of the correlations of flavour, colour longitudinal and transverse momenta between beam remnants[1] and the shower initiators [48, 49], while JIMMY does not consider these correlations. An illustration of p_T scaled multiple interactions is shown in Figure 4.4.

4.1.5   Monte Carlo Event Generators

Concerning the subject of the thesis, which is introduced in the first chapter, various event generators of different orders are used.

AcerMC [50] is a leading order event generator. It is a generator dedicated for the generations of standard model background processes for pp collisions at the LHC. The program provides a library of the massive matrix elements and phase space modules for the generation of selected processes. The generator can be interfaced either PYTHIA [39] or Herwig (Hadron Emission Reactions with Interfering Gluons) [46]. The matrix element codes have been derived using MADGRAPH [51].

MC@NLO is the standard next-to-leading order generator for $t\bar{t}$ studies within the ATLAS Experiment. MC@NLO creates weighted events and the weight can be either $+1$ or -1[2]. MC@NLO allows to incorporate NLO QCD matrix elements consistently into a parton shower framework. With the method described in [52], it

---

[1]The partons, which does not take a active part in the hard scattering process, are called beam remnants.

[2]When quantum amplitudes are summed, interference contributions may be positive, negative or zero. As a consequence, events from MC@NLO might end up having negative weights.
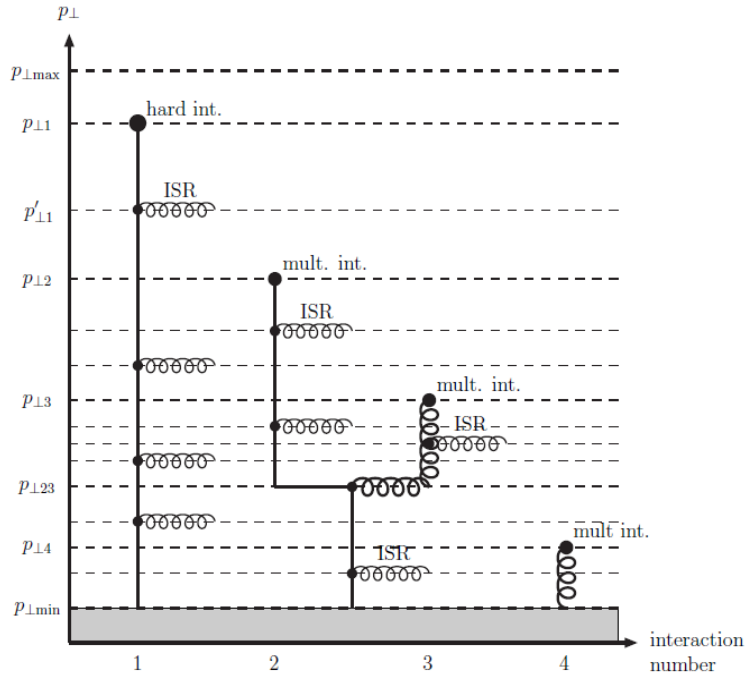
Figure 4.4: Illustration of one incoming hadron in an event with a hard interaction at p_{T_1} and three further interactions at lower p_T scales, each associated with initial-state radiation, and further with the possibility of two interacting partons (2 and 3) having a common ancestor in the parton showers. Most of the activity occurs at small p_T values [49].

is possible to interface the NLO matrix element with parton showers without double counting[1] of partons emitted in soft and hard processes. Double counting can occur both in the final state and in the initial state.

Another NLO generator POWHEG(a Positive Weight Hardest Emission Generator) [53, 54], which is an event generator for heavy quark production in hadronic collisions. Differently from MC@NLO, POWHEG can create unweighted events. It can be interfaced to different shower programs like Herwig and PYTHIA, in such a way that both the leading logarithmic accuracy of the shower and the NLO accuracy are maintained in the output [55].

4.2 Detector Simulation

The outcoming information (truth information) at the end of Monte Carlo event generation phases described above is stored in a container called HepMC. The truth information(MC Truth) stored in the HepMC contains the information of each generated particle including position and four-momentum. MC Truth data is then read by the detector simulation. In this step, the behavior of the detector is simulated. Namely, the bending of particles by the magnetic field in the detector, and their

---

[1]Counting of emissions by both matrix elements and parton shower.
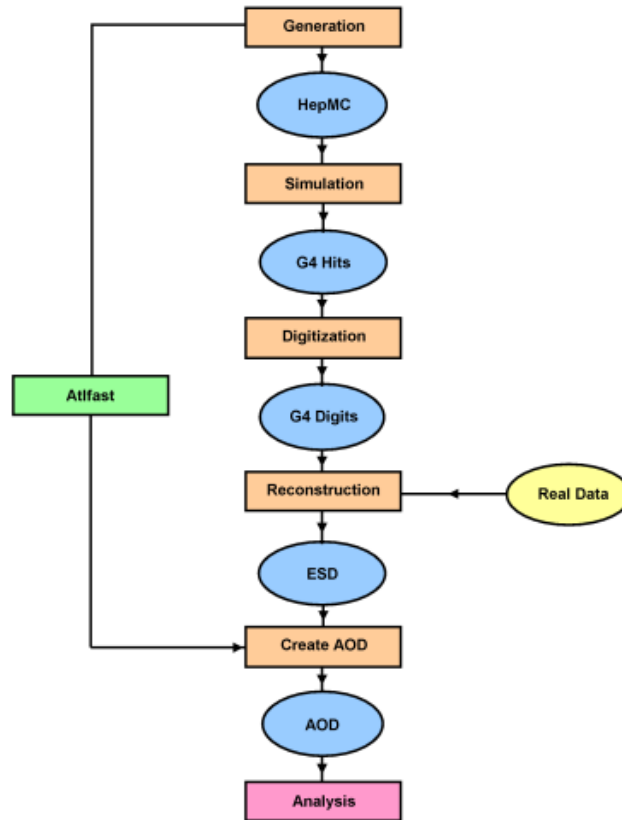
Figure 4.5: ATLAS data simulation flow-chart [56].

interactions with the detector material. At the end of this process, the detector simulation produces 'hits'. The hit information is then passed through the digitization. In the digitization step, the interaction of particles (energy depositions in the calorimeter and the tracks in the inner detector and muon spectrometer) are converted into electronic signals called 'digits'. The collection of the digits, which is called Raw Data Object (RDO), corresponds to the output of the ATLAS detector. The RDOs produced by the detector simulation are used directly by the reconstruction process. A plain flow-chart of the simulation chain can be seen in Figure 4.5.

4.2.1   Detector Simulation with GEANT4

The ATLAS detector simulation is based on GEANT4 [57, 58]. It is a developed version of GEANT3 simulation package, which was used in the preparation of the ATLAS Letter of Intent [59].

GEANT4 is a toolkit, which provides a framework as well as a complete set of tools for detector simulation. The tools are provided for all domains of detector simulation including geometry, tracking, event and track management, detector response and visualization.
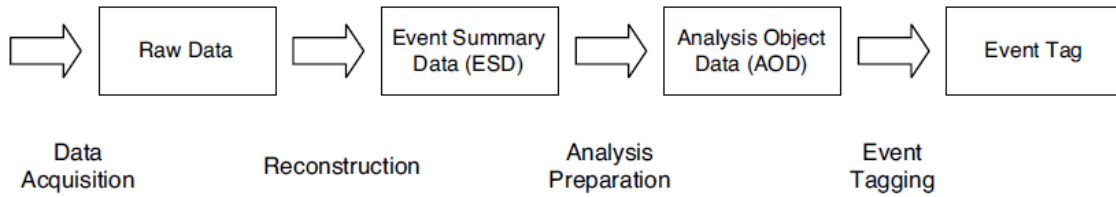
Figure 4.6: Schematic view of the ATLAS event data model [58].

4.2.2 Particle Reconstruction and The ATLAS Event Data Model

The aim of reconstruction is to derive particle parameters and auxilary physics information from the stored raw data [58]. These particle parameters and physics information include photons, electrons, muons, tau-leptons, jets, missing transverse energy, primary vertex, etc.. Information from all detectors is combined to optimize the four-momenta reconstruction for the full momentum and rapidity range. All the hits in the inner detector and in the muon spectrometer as well as the energy depositions in the calorimeters are used to reconstruct the particles. The reconstruction algorithms of the particles which are in consideration of this thesis will be discussed in detail in Section 5.1.

At the end of reconstruction, different types of datasets with different amount of informations are produced to ease the distribution of huge amount of data which will be collected by the ATLAS detector, i.e. 3 PB per year. Starting from the raw data objects, each new generation of data is smaller than the previous generation and each generation includes more specific data for different branches of analyses [60]. A schematic view of the ATLAS event data model can be seen in Figure 4.6.

- **Byte-stream data** is a persistent presentation of the event data flowing from the detector high level trigger.
- **Raw data object data** is a C++ object representation of the byte-stream information.
- **Event summary data** (ESD) contains the detailed output of the detector reconstruction and is produced from the raw data. It contains sufficient information to allow particle identification, track re-fitting, jet calibration etc. The target size for the ESD is 500 kB per event.
- **Analysis object data** (AOD) is a summary of the reconstructed event, and contains sufficient information for common analyses. The target size for the AOD is 100 kB per event.

During the AOD production, event-level metadata (event TAGs) is simultaneously generated. The purpose of such event collections is to support event selection, and later direct navigation to exactly the events that satisfy a predicate (e.g., a cut) on TAG attributes. After all, from the AODs, derived analysis object data (dAOD) can be generated. This data format is also called derived physics data (DPD). The

dAODs are produced by different analysis groups of ATLAS with respect to particular needs of the analysis group. The content of derived physics data is as follows;

- **Derived physics data** [61] is a reduced form of ESD and AOD. With this reduction process, only events that are interesting for the specific types of performance studies or analyses are kept. For particular cases, other captions can be included such as trimming, thinning or slimming. The purpose for DPD is not only to reduce the disk size of the data representation, but also to increase the read speed of the data for any subsequent analysis or performance study.

Another possible option is that users or analysis groups can create secondary (D^2PD) and tertiary (D^3PD) DPDs. D^2PDs and D^3PDs can be created from DPDs as well as directly from AODs. The aim is that each further layer of datasets is more specialized to certain analysis. D^2PDs have to have the same format as ESD, AOD and DPD but D^3PDs can be completely defined by user or analysis groups. The datasets used in this thesis are in D^3PD format and officially produced by the ATLAS top working group.

Chapter 5

Determination of the Systematic Uncertainties

Theoretical predictions need to be confirmed with experimental results of the phenomenon in question. In today's particle physics, the predictions are represented by the use of Monte Carlo generators modeling the physical phenomena that are expected to be observed in experiments.

For this confirmation, it is very important that the theoretical predictions are calculated in detail as much as the phenomena in real life. The scale of detail in Monte Carlo generators is the order at which the matrix element for the relevant process is calculated. The higher the order of the calculation the less possibility for misinterpretation of experimental results. In other words, higher order calculations result in more realistic theoretical prediction and more precise comparison of theory and experiment. Although lowest order corrections can describe general features of a particular process and provide a first estimate of its cross section, in many cases this approximation is not sufficient. The uncertainty in a lowest order calculation originates from its dependence on the unphysical renormalization and factorization scales. Therefore, in order to compare the experimental results with predictions that have smaller theoretical uncertainties, next-to-leading order calculations are imperative for experimental analyses [16].

For the $pp \rightarrow t\bar{t}\gamma$ process, calculations at next-to-leading order QCD corrections to the $t\bar{t}$ pair production associated with a photon in hadron collisions are available [62]. The computation in [62] treats the top quarks as stable particles. But the approximation of [62] can not be used when specific cuts are imposed on top quark decay products. The results of [62] are extended by computing next-to-leading order QCD corrections to the full process $pp \rightarrow t\bar{t}\gamma$, allowing for top quarks to decay [4]. Kinematic distributions for the leptons, which are the decay products of top quark decay in semileptonic channel, as well as the missing transverse energy and the transverse energy distributions for leading order and next-to-leading order calculations [4] are shown in Figure 5.1.
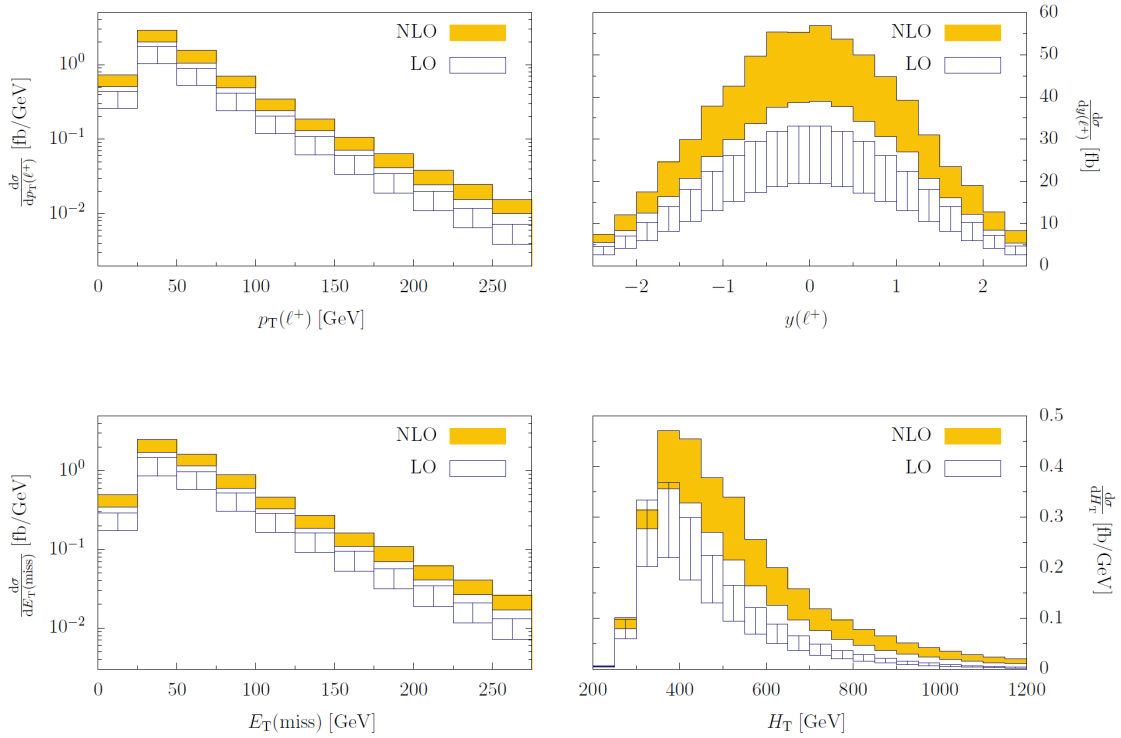
Figure 5.1: Kinematic distributions in $pp \rightarrow (t \rightarrow W^+(l^+\nu)b)(\bar{t} \rightarrow W^-(jj)\bar{b})\gamma$ at the 14 TeV LHC, using specific cuts. The bands correspond to the variation of the renormalization and factorization scales in the interval $m_t < \mu < 2m_t$. Transverse momentum and rapidity distributions of the charged lepton as well as distributions of the missing transverse energy E_T^{miss} and the transverse energy H_T are shown [4].

Although the calculations for next-to-leading order QCD corrections to $t\bar{t}\gamma$ production exist, modeling of these calculations in a Monte Carlo simulation is not available yet. The unavailability of next-to-leading order $t\bar{t}\gamma$ Monte Carlo simulation requires the implementation of a systematic uncertainty for the signal efficiency in the analysis. This uncertainty will be determined by comparing Monte Carlo samples for top quark pair production of different orders. This chapter presents the determination of this systematic uncertainty.

5.1 Object Reconstruction Algorithms and Object Definitions

5.1.1 Reconstruction Algorithms

Electron Reconstruction

The reconstruction of electrons [63] in ATLAS is done depending on the signal produced by the inner detector and the electromagnetic calorimeter. The track reconstruction in the inner detector is done in a coverage up to $|\eta| < 2.5$. The elec-

tromagnetic calorimeter provides the measurement of the longitudinal extension of the electromagnetic shower. The reconstruction usually starts with the independent reconstructions of tracks from the inner detector and electromagnetic clusters from the cells of the calorimeter.

The track reconstruction involves two algorithms. The first, *inside-out* algorithm, starts from seeds in the layers of the pixel detector and SCT and then finds the hits in the TRT. The second algorithm, *back-tracking*, starts from the hits in the TRT and extrapolates them to the SCT and pixel detector layers. Both use track fitters taking into account the fraction of energy radiated in the inner detector by bremsstrahlung processes.

The reconstruction of electromagnetic clusters uses an algorithm called *sliding-window*. In this algorithm, a $\eta - \phi$ space (window) of chosen calorimeter cells (within given η boundaries) is divided into a grid of $N_\eta \times N_\phi$ elements of size $\Delta_\eta \times \Delta_\phi$. The given η boundaries for electron reconstruction is η=0.025. Inside each of the elements, the energy of all cells in all longitudinal layers is summed into the 'tower' energy. Then, a seed is formed if the transverse energy in the window is greater than a defined threshold, which is 3 GeV for electrons. The *sliding-window* algorithm is also used for jet reconstruction in the calorimeter (see Section 5.1.1).

After all, the tracks reconstructed in the inner detector are matched to the clusters reconstructed in the calorimeter. In case, multiple tracks are associated to one cluster, the association is done with the track giving the ratio $E_{cluster}/p_{track}$ closest to 1. Due to the high event rate of the LHC at its nominal luminosity, a large number of jets and pile up events faking electrons exist. Therefore, a powerful method for the reconstruction and efficient criteria for the identification are important.

Muon Reconstruction

In the ATLAS experiment there are three different strategies and corresponding algorithms for muon reconstruction. The first strategy is called standalone reconstruction, which uses only muon spectrometer information. The second is combined muon reconstruction, which combines the standalone muon tracks with the tracks reconstructed in the inner detector. The last algorithm is a tagging algorithm which tags the inner detector tracks using calorimeter and muon spectrometer information. In addition to reconstruction algorithms, there are two reconstruction methods in ATLAS. Each method is comprised of several algorithms which covers all three strategies and they are called MuID and Staco [64]. The muons used in this analysis are required to be reconstructed with respect to the MuID method which uses the combined muon reconstruction algorithm.

The starting point of standalone track reconstruction in the muon spectrometer is a search for patterns among hits. In the selected areas, segments are produced by fitting close hits in the same chamber. These segments are used to perform a fit of a

whole track. The tracks are then extrapolated back to the interaction point taking into account energy loss and multiple scattering in the calorimeter.

The combined reconstruction algorithm matches the standalone muon tracks extrapolated back to the vertex with the inner detector tracks within the coverage of $|\eta| < 2.5$. After matching, a combined single track is produced, in order to take advantage of the complementary momentum sensitivities of muon spectrometer and the inner detector over the whole p_T range.

Tagged muons are additional muon candidates which are obtained by tagging inner detector tracks with muon spectrometer or calorimeter measurements. This strategy can recover both low energy muons and muons in areas with limited muon spectrometer coverage, since it is less sensitive to Coulomb scattering and energy loss. This strategy helps also detector commissioning.

Jet Reconstruction

A jet is defined as a cluster of energy depositions and tracks that collision products leave within the calorimeter and inner detector. Algorithms for clustering jets [65,66] are very important tools for analyzing data from hadronic collisions. A jet algorithm defines how signals in the detector, or partons in a generator are clustered into jets. They associate the kinematic properties of partons to the kinematic properties of jets.

Different jet algorithms, which have different approaches, can be mainly grouped in two subgroups; cluster algorithms and cone algorithms. The latter is not described here, since in this analysis only the jets reconstructed with cluster algorithms are used.

Cluster Algorithm

As input for cluster algorithms, there are two approaches. The first approach uses four-vectors, that represents the energy deposition in calorimeter towers. The other approach, which is the standard choice in ATLAS, uses topological clustering. The essential idea of topological clustering is to group into clusters neighboring cells that have significant energies compared to the expected noise. One of the mostly used cluster algorithm is the k_t algorithm [67,68]. For this algorithm, the distance measurement between particles or pseudojet is defined as:

$$d_{ij} = min(k_{ti}^{2p}, k_{tj}^{2p})\frac{\Delta_{ij}^2}{R^2}, \tag{6.1a}$$

$$d_{iB} = k_{ti}^{2p}, \tag{6.1b}$$

where $\Delta_{ij}^2 = (y_i - y_j)^2 + (\phi_i - \phi_j)^2$ and d_{ij} is the distance between two objects (i and j), and d_{iB} is the distance between the object i and the beam B. k_{ti}, y_i and
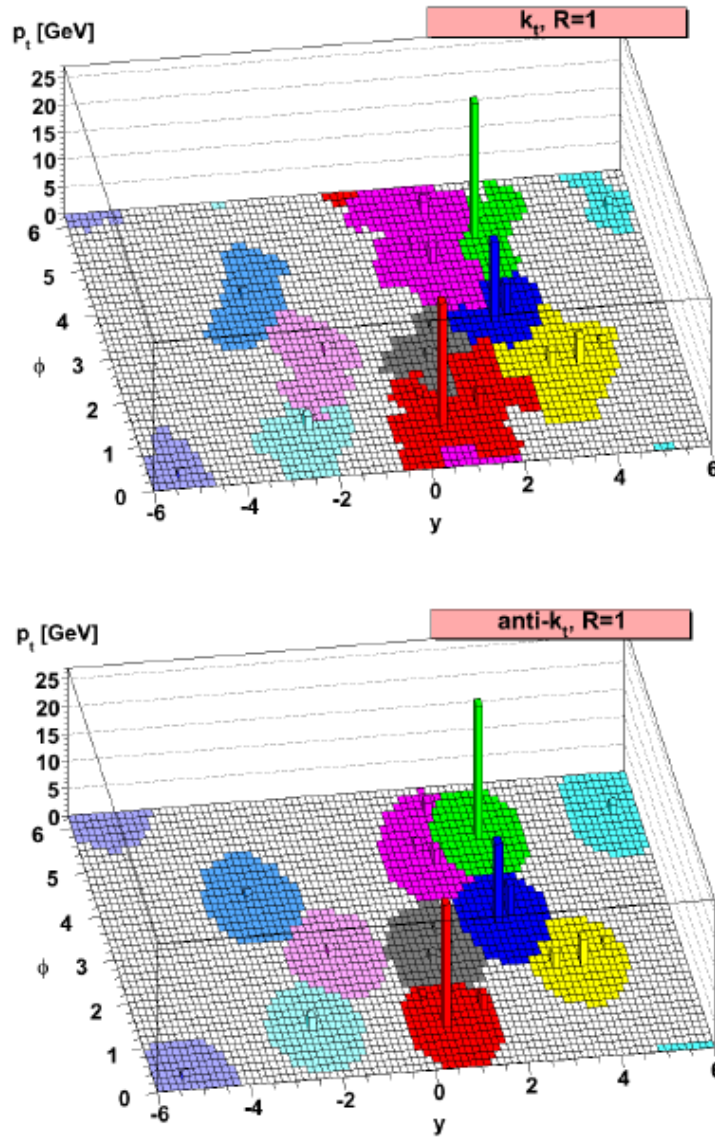
Figure 5.2: A sample parton-level event clustered with two different jet algorithms, illustrating shape of the jets with k_T algorithm (upper) and anti-k_T algorithm (lower) [65].

ϕ_i are the transverse momentum, rapidity and azimuth angle of i, respectively. In addition to the usual radius parameter R, another parameter p is added to deal with the relative power of the energy versus Δ_{ij} scales.

For $p=1$ the inclusive k_t algorithm is recovered. The case of $p=0$ is special and it corresponds to the inclusive Cambridge/Aachen algorithm [69, 70], while the case of $p=-1$ corresponds to the anti-k_t jet-clustering algorithm.

The anti-k_t algorithm combines first the objects with high p_T. The essential feature of the algorithm is that the shape of jets is modified by hard jets instead of soft jets. As a consequence perfectly conical jets are obtained. Differences between

the anti-k_t and the k_t algorithm can be seen in Figure 5.2. The jets used in this analysis are reconstructed with the anti-k_t jet clustering algorithm.

5.1.2   Object Definitions

According to the reasons explained in the analysis strategy, the proper objects to compare different Monte Carlo samples are electrons, muons and jets. In this section, the definitions of these objects are described [36].

Electrons

Electrons are required to have p_T>25 GeV and $|\eta_{cluster}|$<2.47, where $\eta_{cluster}$ is the pseudorapidity of the electromagnetic cluster associated with the electron. Electrons in the crack region 1.37<$|\eta_{cluster}|$<1.52 are excluded. The reconstruction algorithm for the electron must be track-based or, both track-based and cluster-based at the same time. Pile-up corrected and p_T-corrected [71] etcone20[1] must be smaller than 3.5 GeV. Finally, the electrons must be tight[2] and the dead OTX regions must be avoided [73]. Additionally, jets within ΔR = 0.2 of an electron are removed to avoid double counting[3].

Muons

Muons are reconstructed with combined reconstruction algorithm (author==12) which is previously explained in Section 5.1.1. Transverse momentum for muons is required to be p_T>20 GeV and pseudorapidity $|\eta|$<2.5. As the isolation cut, etcone30 and ptcone30 must be smaller than 4 GeV. Muons within a ΔR = 0.4 cone of a jet with $p_T > 20$ GeV are removed in order to reduce the contamination caused by muons from hadron decays.

Jets

Jets are reconstructed by the anti-k_t algorithm (See Section 5.1.1) with a radius of R=0.4. The reconstruction starts from the energy clusters of adjacent calorimeter

---

[1]The etcone calorimeter isolation variables are calculated by taking a simple sum of calorimeter cell energies inside of a cone of a certain radius around the cluster barycenter, excluding a 5x7 grid of cells in the center of the cone.

[2]The baseline electron identification in ATLAS relies on cuts using variables that provide good separation between isolated electrons and jets (faking electrons). These variables include calorimeter, tracker and combined calorimeter/tracker information. Cuts on these variables can be applied independently. Three reference sets of cuts have been defined: loose, medium and tight. This provides flexibility in analyses, for example to improve the signal efficiency for rare processes which are not subject to large backgrounds from fakes. Typically shower shape variables of the second calorimeter layer and hadronic leakage variables are used in the loose selection. First calorimeter layer cuts, track quality requirements and track-cluster matching are added at the level of the medium selection. The tight selection adds E/p, b-layer hit requirements and the particle identification potential of the TRT [72].

[3]Electron clusters can also be reconstructed as a jet.

cells. The closest jet to an accepted[1] electron within a cone of $\Delta R{<}0.2$ is removed. Additionally, only jets with $p_T{>}20$ GeV and $|\eta|{<}2.5$ are selected.

5.2   Analysis Strategy

As introduced in the beginning of this chapter, the strategy relies on the comparison of samples of different order, i.e. leading order and next-to-leading order. This comparison is done using the efficiency which will be explained below. As a NLO $t\bar{t}\gamma$ sample is not available, the systematic uncertainty is determined comparing $t\bar{t}$ samples at LO and NLO. For this purpose, the default leading order sample and the default next-to-leading order sample for $t\bar{t}$ studies, which are officially produced by ATLAS top working group, are chosen. These samples are produced with AcerMC and MC@NLO, respectively. As already described in Chapter 4, production of a Monte Carlo data sample consists of mainly two stages, i.e. generation of events and showering of events. These event generators above can be interfaced to any parton shower program but AcerMC is usually interfaced to PYTHIA and MC@NLO to Herwig. Since the main concern is to observe the differences between the samples generated at different orders, comparison of these samples, which are showered with different parton showers, is not proper enough. The reason behind this is that each parton shower algorithm has an individual algorithm. This means that handling of physics phenomena differs, e.g. ordering of evolution variable for initial- and final-state radiations (see Section 4.1.2). This divergence between the showering phase of the samples plays an important role in the characterization of the analysis strategy. Concerning this divergence, a transition phase from AcerMC+PYTHIA to MC@NLO+Herwig is needed and this is possible with another next-to-leading sample which is showered using PYTHIA like AcerMC. Among the officially produced $t\bar{t}$ samples, POWHEG+PYTHIA is chosen for this transition. With this phase, the analysis is separated into two steps. In the first step, instead of a comparison between AcerMC+PYTHIA and MC@NLO+Herwig, the comparison between AcerMC+PYTHIA and POWHEG+PYTHIA is done. Then in the second step, as a comparison of parton showers, the two next-to-leading samples POWHEG+PYTHIA and MC@NLO+Herwig are compared. This strategy will yield two different uncertainties to implement.

Another issue is the physical observables to be used for the comparison of different event generators. Direct comparison of top quarks from the event record of the generators is not recommended. Specifically speaking, top quarks in the POWHEG+ PYTHIA event record are boosted to the lab frame after final state radiation and hadronisation processes. On the other hand, in the MC@NLO+Herwig sample, none of the top quarks are boosted to the lab frame [74]. Therefore, the kinematic properties of the top quarks can not be directly compared. Instead, to compare the decay

---

[1]See electron selection section 5.1.2

products in the final state of $t\bar{t}$ is the proper way. As described in the Section 3.1.4 the final state of the $t\bar{t}\gamma$ process is $t\bar{t}\gamma \to l^{\pm}\nu b\bar{b}jj\gamma$. The event selection for the $t\bar{t}\gamma$ is given below. In the event selection cut flow, the cuts up to C17 are the cuts for $t\bar{t}$ process and the rest are additional cuts for the $t\bar{t}\gamma$ process, since the final states of these two processes are quite similar. Since in the analysis the $t\bar{t}$ final state is used for the comparison, leptons and jets in the final state are reasonable to use. Therefore, each step of the analysis is separated into two parts. The first part is the comparison of stable leptons and this part is performed for electron and muon channel separately. Second part is the comparison of jets. The definitions of the objects, that are used in the analysis are described in Section 5.1.2.

The comparison between the samples is done depending on efficiencies which are calculated with respect to the event selection cut flow. Namely, first the selection efficiencies with respect to leptons and jets are calculated and then the relative difference is determined as a systematic uncertainty. The event selection cut flow for semileptonic channel is as follows:

1. **C1:** Jet is safe. *(Cut due to the LAr hole.)*

2. **C2:** Required electron(muon) trigger for the e+jets (μ+jets) channels fired.

3. **C3:** The first primary vertex must be reconstructed with more than four tracks originating from it.

4. **C4:** The event has to contain at least one electron with $p_T > 25$ GeV or at least one muon with $p_T > 20$ GeV.

5. **C5:** The event has to contain exactly one electron with $p_T > 25$ GeV or exactly one muon with $p_T > 20$ GeV.

6. **C6:** The event has to contain no muon with $p_T > 20$ GeV in the e+jets channel or no electron with $p_T > 25$ GeV in the μ+jets channel.

7. **C7:** The selected lepton is required to match the trigger lepton.

8. **C8:** The event is rejected if the electron shares a track with a muon close to a jet (e/μ overlap).

9. **C9:** Jet Cleaning: no bad jets[1] with $p_T > 20$ GeV.

10. **C10:** Missing transverse energy cut: $\not{E}_T > 35$ GeV in the e+jets and $\not{E}_T > 20$ GeV in the μ+jets channel.

11. **C11:** Transverse $W^{\pm}$ boson mass cut: $\not{E}_T + M_T^{W^{\pm}} > 60$ GeV (triangular cut) in the μ+jets channel or $M_T^{W^{\pm}} > 25$ GeV (box cut) in the e+jets channel.

12. **C12:** At least two jets with $p_T > 25$ GeV, $|\eta| < 2.5$.

13. **C13:** At least three jets with $p_T > 25$ GeV, $|\eta| < 2.5$.

14. **C14:** At least four jets with $p_T > 25$ GeV, $|\eta| < 2.5$.

---

[1]Bad jet definition is based on several variables such as: energy fraction in the HEC, maximum energy fraction in one calorimeter layer, etc.. For further reading, see [75].

15. **C15:** At least one good jet ($p_T > 25$ GeV and $|\eta| < 2.5$) with secondary-vertex (SV0) weight > 5.85.

16. **C16:** Events with noise based on LAr-Detector are removed.

17. **C17:** At least one photon with $p_T > 15$ GeV, $|\eta| < 2.5$.

18. **C18:** Transverse $e + \gamma$ mass cut: Events with 86.0 GeV $\leq M_{e+\gamma}^{inv} < 96.0$ GeV (Z boson mass region) are removed.

19. **C19:** Events with a photon-jet overlap within $\Delta R < 0.5$ are removed.

Depending on the case, i.e. lepton case or jet case, an efficiency is calculated. In each case, different cuts are used. The strategy to select the cuts will be described in details in the following sections. The final step of the uncertainty determination is the calculation of the relative difference between the calculated efficiencies.

5.3   AcerMC+Pythia and POWHEG+Pythia

In this section the comparison between AcerMC+Pythia and POWHEG+Pythia is performed as the first part of the analysis. As mentioned before the analysis for leptons is done for electron and muon channel separately.

5.3.1   Leptons

As mentioned in the analysis strategy, the determination of the uncertainty relies on efficiencies of objects which are selected to be used. In this part, the systematic uncertainty determination regarding electrons and muons is done. For electrons and muons, the efficiency is calculated with respect to the cut C7, where the selected lepton matches the required lepton trigger. The lepton trigger for e^-+Jets channel is EF_e20_medium and EF_mu18 for μ+Jets. EF stands for Event Filter, the numbers 18 and 20 for required p_T and medium for the electron cut criteria which is explained above in the footnote. For the purpose of this analysis, the lepton efficiency is defined as

$$\epsilon = \frac{N_{e^-,\mu^-}^{reco}}{N_{e^-,\mu^-}^{true}}, \tag{5.1}$$

where N_{e^-,μ^-}^{reco} is the number of reconstructed electrons or muons selected after cut C7 and the N_{e^-,μ^-}^{true} is the number of true electrons or muons at the generator level. For reconstructed leptons, an additional geometrical truth matching is applied. Due to this, only the reconstructed lepton, that is closest to the true lepton within a cone of size $\Delta R=0.1$, is selected. In case, there is no electron within the defined cone for matching, the event is skipped.

According to this selection strategy, the kinematic distributions of selected objects are obtained. In Figure 5.3, the upper and middle histograms show the trans-

verse momentum distributions of true and reconstructed electrons, respectively. Distributions are shown for the leading order sample AcerMC and next-to-leading order sample POWHEG. The lower histogram shows the efficiency as a function of p_T. In Figure 5.4, the upper and middle histograms show the pseudorapidity distributions of again the true and the reconstructed electrons, respectively. For each data sample, $\sim$1,000,000 events are used and the histograms are normalized to same luminosity, which is 1 fb^{-1}. Consequently, excepting the p_T cut for reconstructed electrons due to the event selection at 25 GeV, only a few differences can be seen between the samples:

- The p_T distributions (Figure 5.3) for the leading order sample AcerMC both for true and reconstructed leptons are slightly harder than that of the next-to-leading order sample POWHEG.

- As a consequence of having a harder p_T distribution, the η distributions for the leading order sample AcerMC are expected to be slightly narrower than next-to-leading order sample POWHEG, as it can be observed in Figure 5.4.

The efficiencies both for p_T and η distributions are calculated bin per bin. The efficiency errors are calculated with respect to the binomial model [76]. According to this model, the number of selected events, e.g., m, is considered as a binomially distributed variable, i.e., one finds m 'successes' out of N independent trials, where the probability of success on each trial is the efficiency ϵ. Finally the model estimates the error efficiency to be calculated as follows:

$$\sigma = \sqrt{\frac{\epsilon(1-\epsilon)}{N}}. \tag{5.2}$$

Efficiency distributions as a function of both p_T and η can be seen in Figures 5.3 and 5.4, respectively. The electron efficiencies for AcerMC and POWHEG are in agreement except for statistical fluctuations in the large p_T region. For the case of muons, the same strategy as for the electrons is applied. Kinematic distributions for muons can be seen in Figures 5.5 and 5.6, respectively. Except for the p_T cut at 20 GeV, the kinematic distributions for true muons and reconstructed muons show again only minor differences. As for the electrons, the p_T distribution is harder for AcerMC compared to POWHEG sample, besides the narrower η distribution for AcerMC compared to the POWHEG. A remarkable point, which is seen in the p_T distribution of reconstructed muons, is the cut at 150 GeV. As a consequence of a combined muon trigger bug in MC, the scale factor[1] (SF) vs p_T is not known in the region above 150 GeV. Due to this, the events with a muon with p_T>150 GeV must be removed [77]. The η distributions for reconstructed electrons and muons also have differences. In Figure 5.6, the fluctuations of the efficiency for reconstructed

---

[1]Scale factors are data driven factors for physical quantities e.g, momentum and energy of particles, to scale the Monte Carlo values to data values.

Figure 5.3: The upper histogram shows the p_T distribution of true electrons before all cuts for AcerMC + Pythia and POWHEG + Pythia. The second one shows the p_T distribution of reconstructed electrons selected after the last lepton cut and truth matching. The lower histogram shows the efficiencies for the electron selection for the two samples.
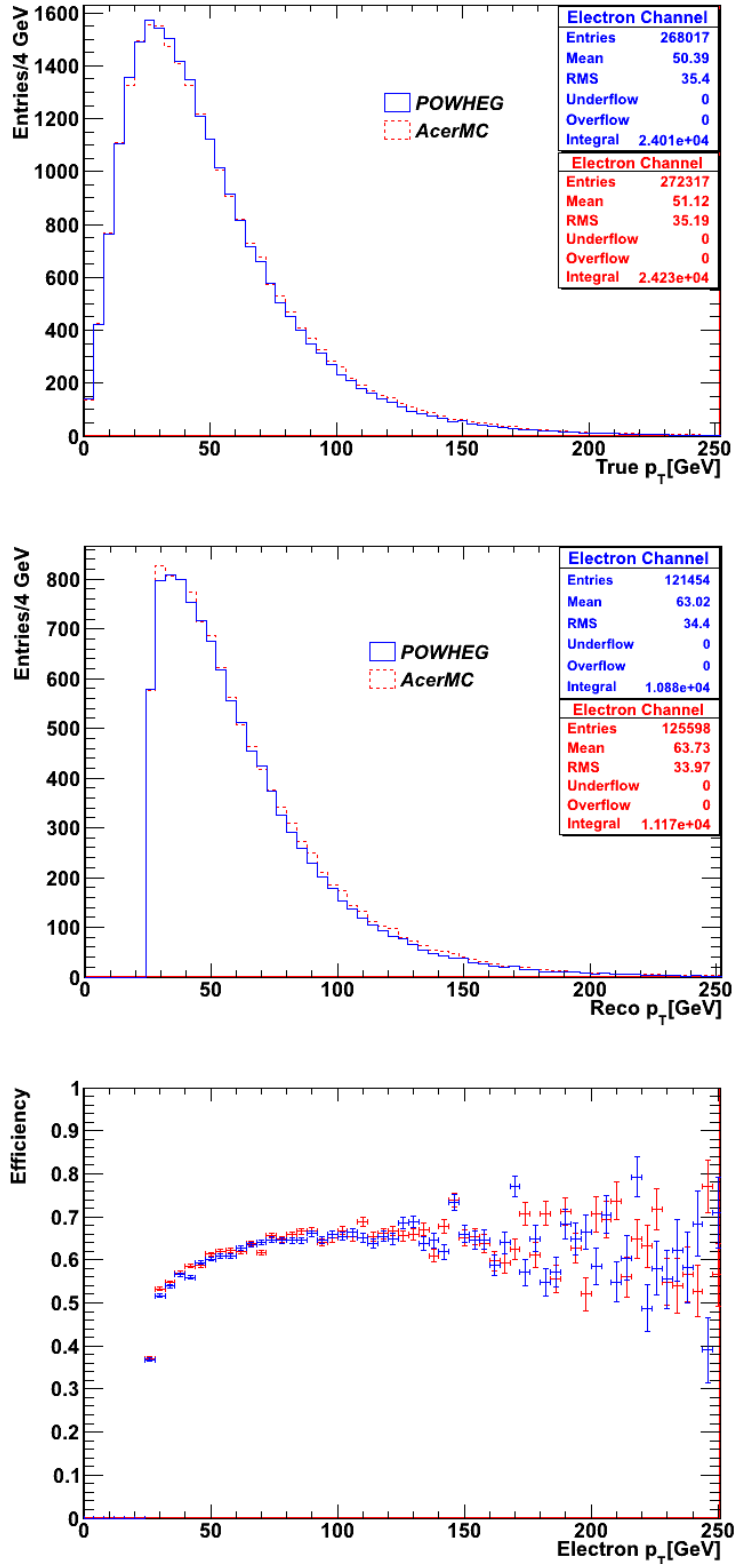
Figure 5.4: The upper histogram shows the η distribution of true electrons before all cuts for AcerMC + Pythia and POWHEG + Pythia. The second one shows the η distribution of reconstructed electrons selected after the last lepton cut and truth matching. The lower histogram shows the efficiencies for the electron selection for the two samples.
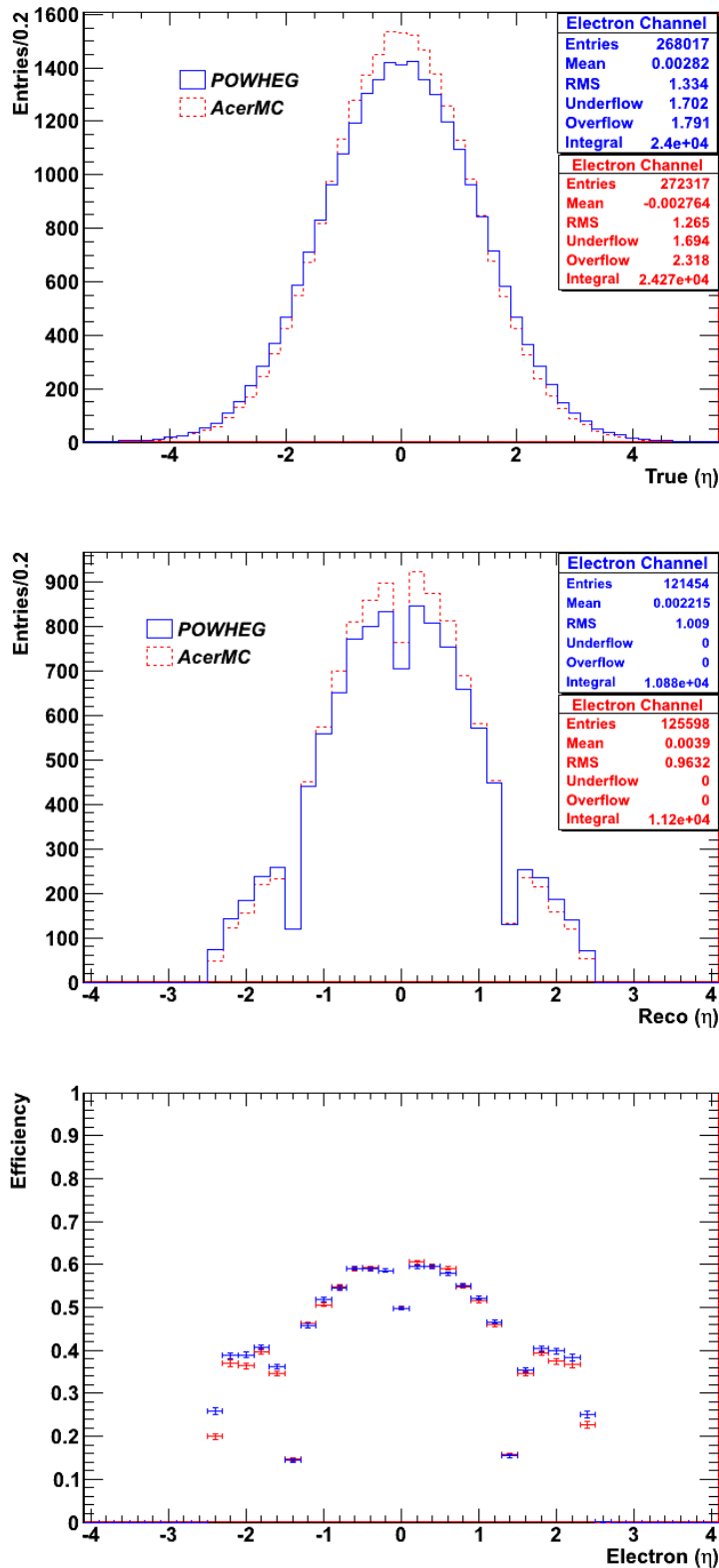
muons in the barrel region are a consequence of the reduced geometrical coverage of the RPC detectors close to the feet of the toroidal magnet support structure. Consequently the efficiency is lower in the barrel region.

The numerical values of the calculated selection efficiencies are shown in Table 5.1. As can be observed, both in distributions and from numerical values, the efficiencies for AcerMC+PYTHIA and POWHEG+PYTHIA are close to each other and do not have large differences. The results are also confirmed by the plots.

As mentioned before, the main aim is to determine the differences of the efficiencies of the two samples as a systematic uncertainty. In order to do this, the relative difference between the efficiencies has to be calculated. The formula to calculate the relative difference is as follows:

$$\frac{\varepsilon_1 - \varepsilon_2}{(\varepsilon_1 + \varepsilon_2)/2}, \tag{5.3}$$

where ε_1 and ε_2 are the efficiencies for the different samples. For the calculation of the uncertainty errors, the usual error propagation rule is used. The calculated differences are shown in Table 5.2. The calculated numbers show that the systematic uncertainties due to the leptons are remarkably small, i.e., less than 2%.

Table 5.1: Lepton Efficiencies For AcerMC + PYTHIA and POWHEG + PYTHIA

	AcerMC	POWHEG
e Channel	0.461±0.003	0.453±0.003
μ Channel	0.446±0.003	0.451±0.003

Table 5.2: Relative Difference of Lepton Efficiencies

	AcerMC-POWHEG
e Channel	0.017±0.01
μ Channel	0.010±0.01

5.3.2 Jets

In order to be able to calculate the jet efficiency, the cuts involving jets have to be considered. In this case, the efficiency is calculated with respect to cut C11 and C14. As described in Section 3.1.3, in the lepton+jets channel at least four jets are required. In the event selection cutflow, the cut C11 is the last before the jet selection starts and C14 is the last one for the jet selection. For the efficiency calculation in this analysis, the cut for b-tagged jet is not considered. Also, all bad jets are removed before cut C11.

Figure 5.5: The upper histogram shows the p_T distribution of true muons before all cuts for AcerMC + PYTHIA and POWHEG + PYTHIA. The second one shows the p_T distribution of reconstructed muons selected after the last lepton cut and truth matching. The lower histogram shows the efficiencies for the muon selection for the two samples.
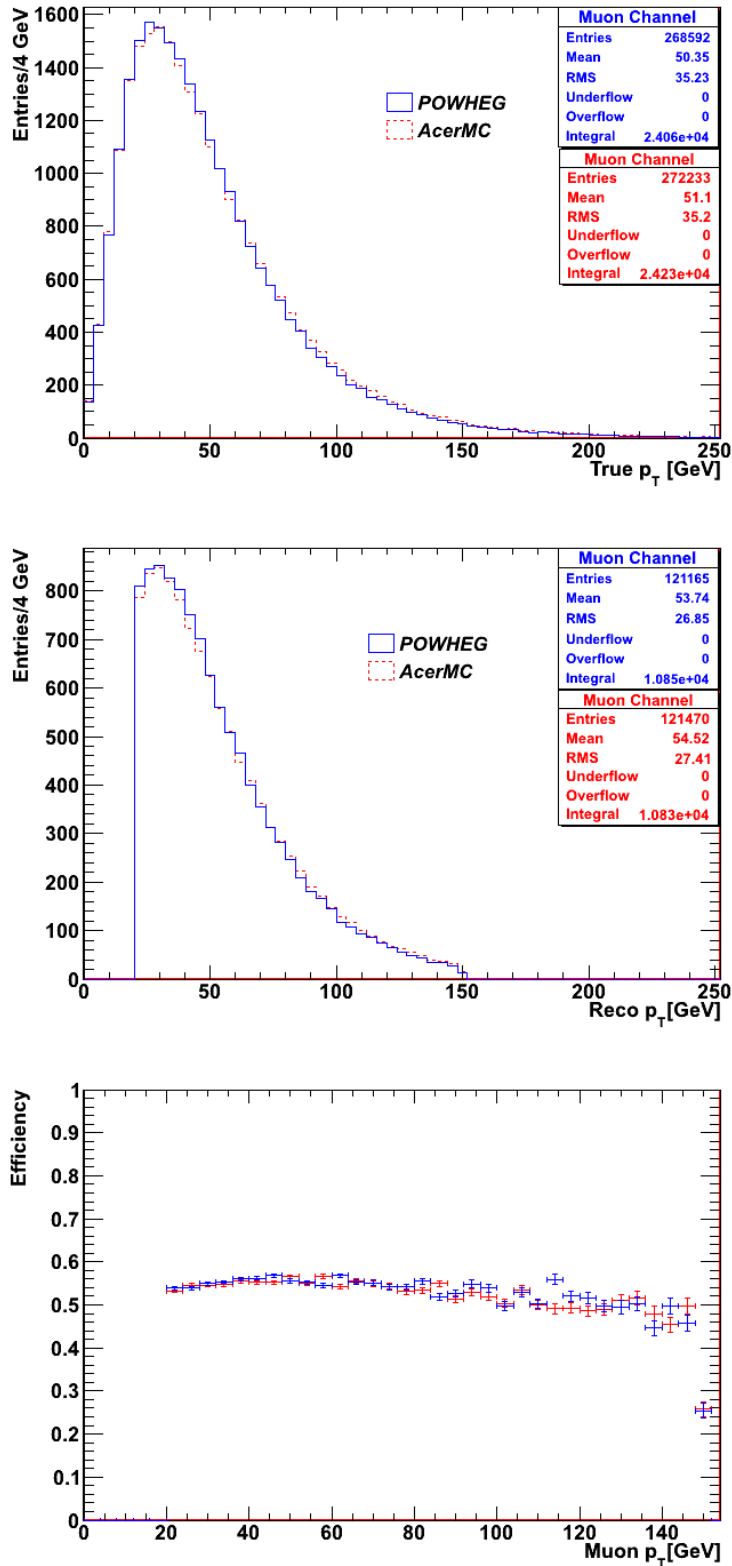
Figure 5.6: The upper histogram shows the η distribution of true muons before all cuts for AcerMC + Pythia and POWHEG + Pythia. The second one shows the η distribution of reconstructed muons selected after the last lepton cut and truth matching. The lower histogram shows the efficiencies for the muon selection for the two samples.
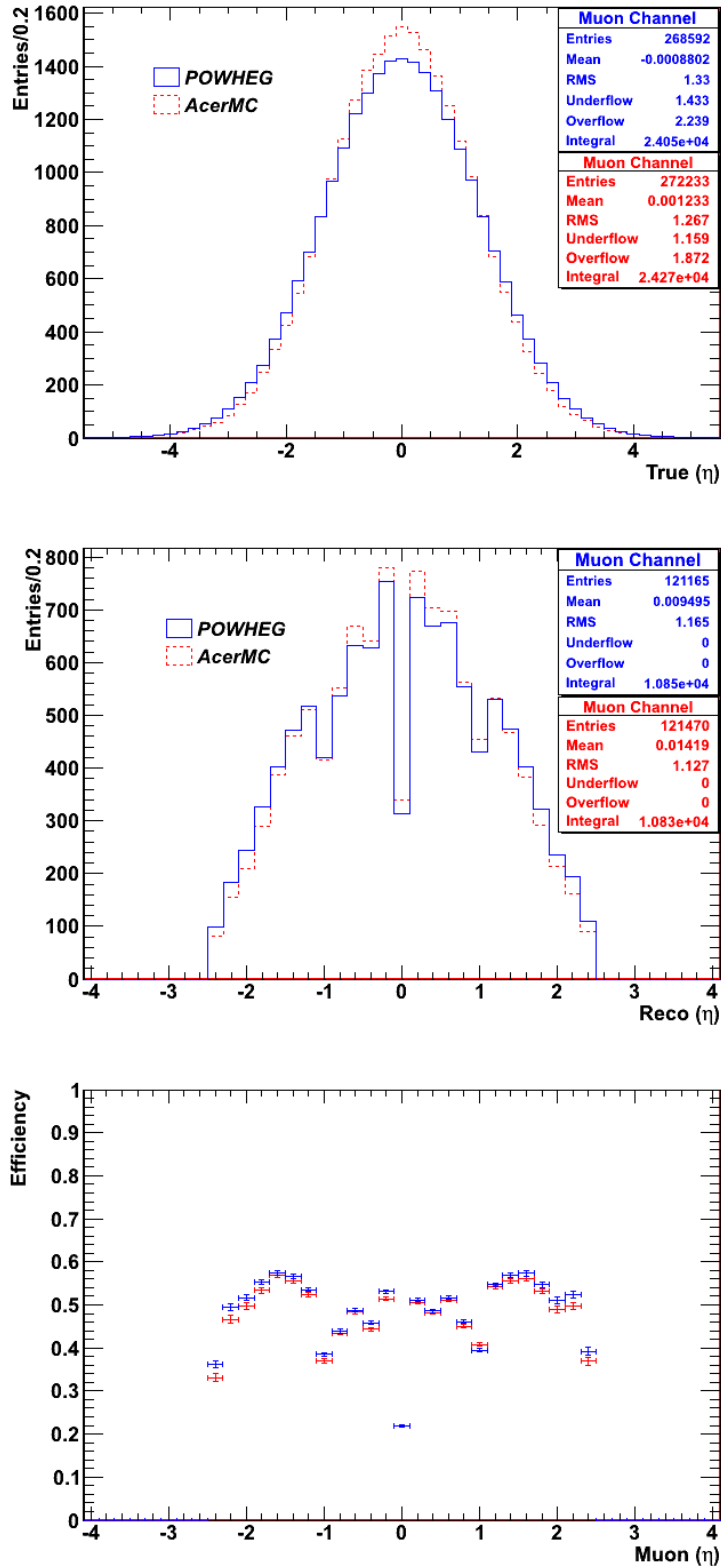
For the event selection of the jet efficiency calculation, only reconstructed jets are used both at cut C11 and C14. As in the lepton case, a geometrical truth matching is applied. Since there are four jets in the final state of the lepton+jets channel, the geometrical truth matching is applied to the four jets which have the highest p_T. The cone size is the same as for the matching applied in lepton case which is $\Delta R = 0.1$.

According to the cut based and truth matching selection, only the events, in which the first four jets with highest p_T are matched to true jets, are considered. This selection is done for both cut C11 and C14. For the comparison of the kinematic distributions and the efficiency calculation, only the highest p_T jet is shown. The jet analysis is performed for e+jets and μ+jets separately.

In Figure 5.7 the transverse momentum distributions of the highest p_T jet for the e+jets channel can be seen. The first histogram shows the p_T distribution of jets selected after C11 and the second histogram shows the p_T distribution of jets selected after C14. The lower histogram shows the efficiency of the jet selection as a function of the jet p_T. As for leptons, the p_T distribution of AcerMC is harder than that of POWHEG but the difference of hardness is larger for the jets compared to lepton p_T distributions. The η distribution for the jets in the AcerMC sample is slightly narrower than that for POWHEG. The kinematic distributions of jets for the μ+jets channel are shown in Figures 5.9 and 5.10.

Table 5.3: Jet Efficiency For AcerMC and POWHEG

	AcerMC	POWHEG
e Channel	0.675±0.005	0.657±0.006
μ Channel	0.701±0.005	0.681±0.005

Table 5.4: Relative Difference of Jet Efficiencies for AcerMC and POWHEG

	AcerMC-POWHEG
e Channel	0.026±0.012
μ Channel	0.029±0.010

Figure 5.7: The upper histogram shows the p_T distribution of reconstructed jets in the e^-+jets channel before the cut C12 for AcerMC + Pythia and POWHEG + Pythia. The second one shows the p_T distribution of reconstructed jets after cut C14. The lower histogram shows the efficiencies for the jet selection for the two samples.
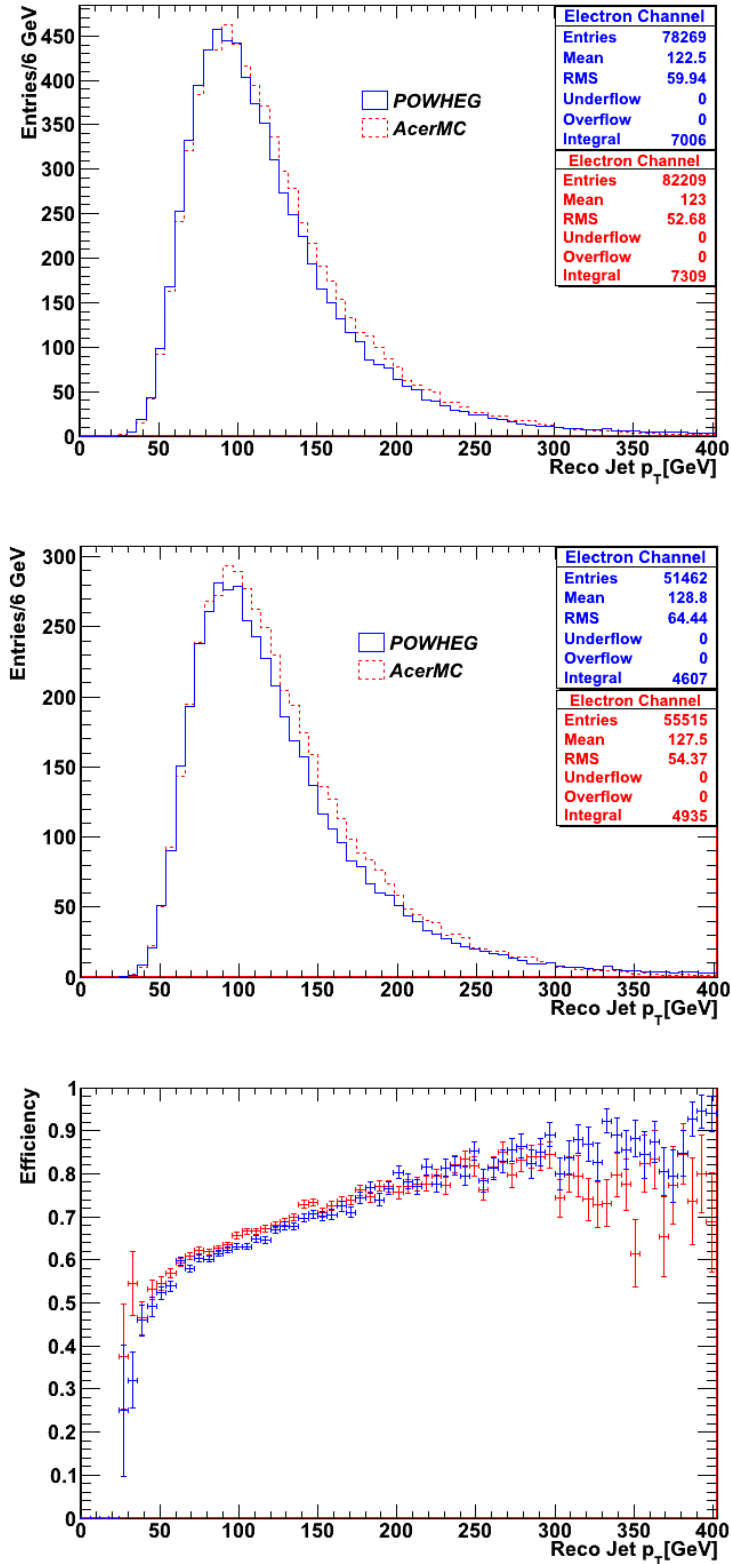
Figure 5.8: The upper histogram shows the η distribution of reconstructed jets in the e^-+jets channel before the cut C12 for AcerMC + PYTHIA and POWHEG + PYTHIA. The second one shows the η distribution of reconstructed jets after cut C14. The lower histogram shows the efficiencies for the jet selection for the two samples.
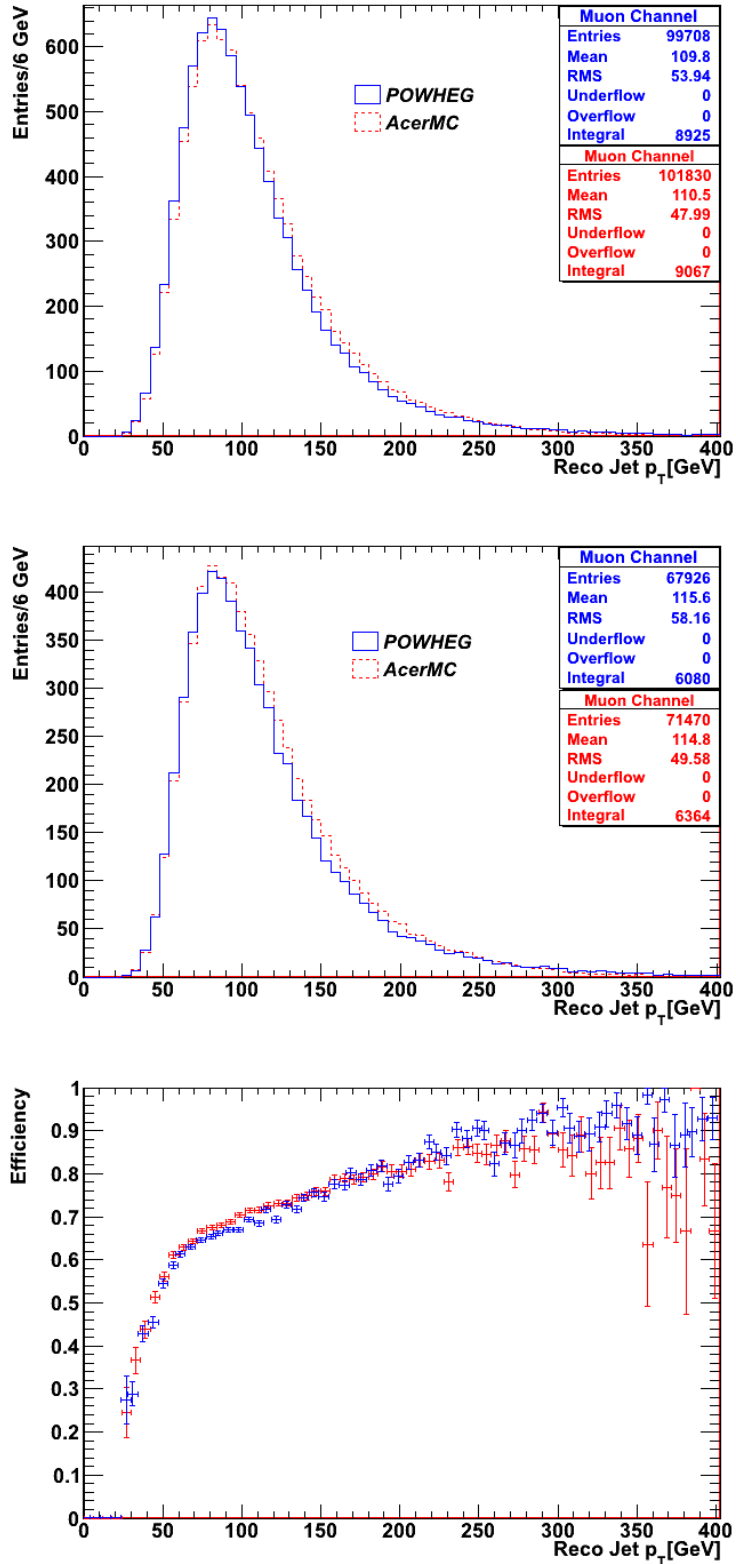
Figure 5.9: The upper histogram shows the p_T distribution of reconstructed jets in the μ+jets channel before the cut C12 for AcerMC + Pythia and POWHEG + Pythia. The second one shows the p_T distribution of reconstructed jets after cut C14. The lower histogram shows the efficiencies for the jet selection for the two samples.
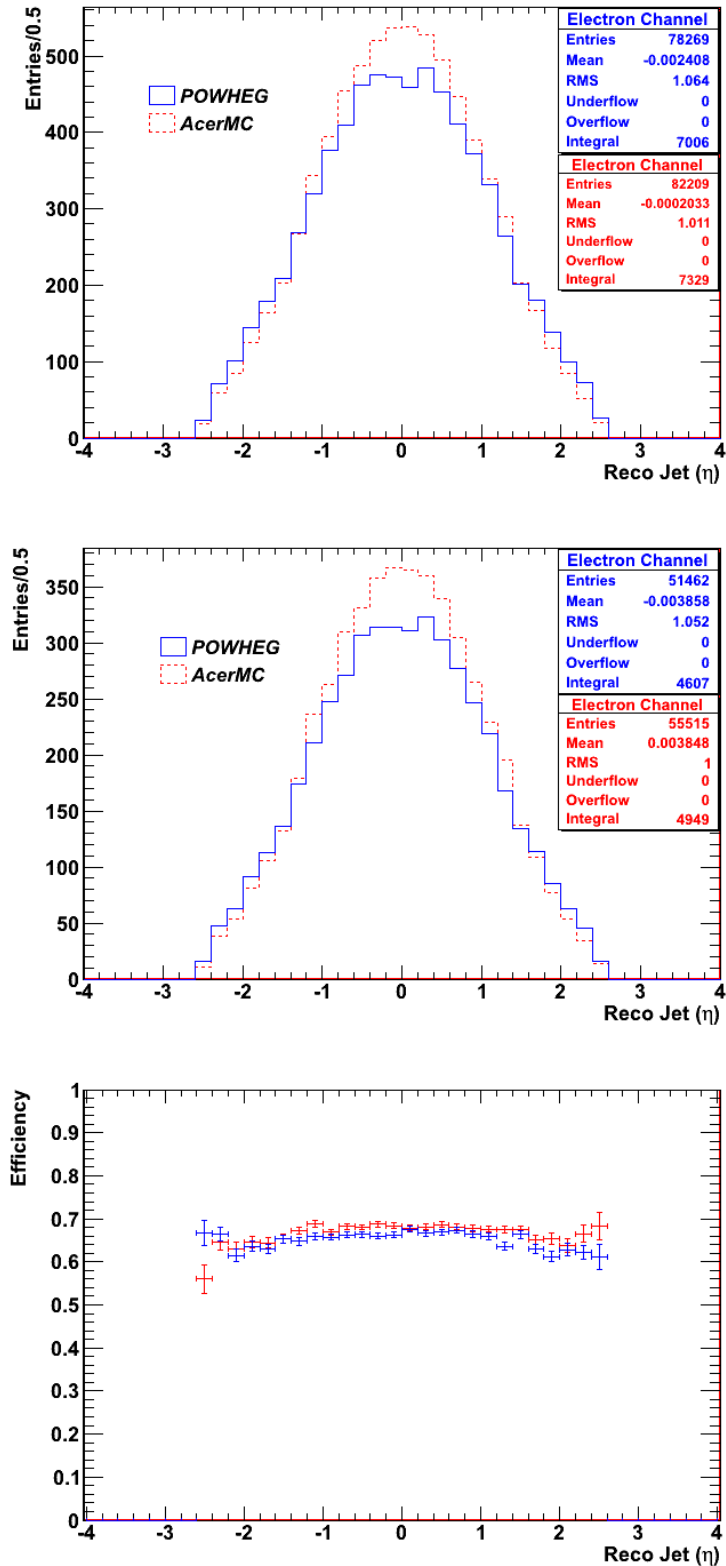
Figure 5.10: The upper histogram shows the η distribution of reconstructed jets in the μ+jets channel before the cut C12 for AcerMC + Pythia and POWHEG + Pythia. The second one shows the η distribution of reconstructed jets after cut C14. The lower histogram shows the efficiencies for the jet selection for the two samples.
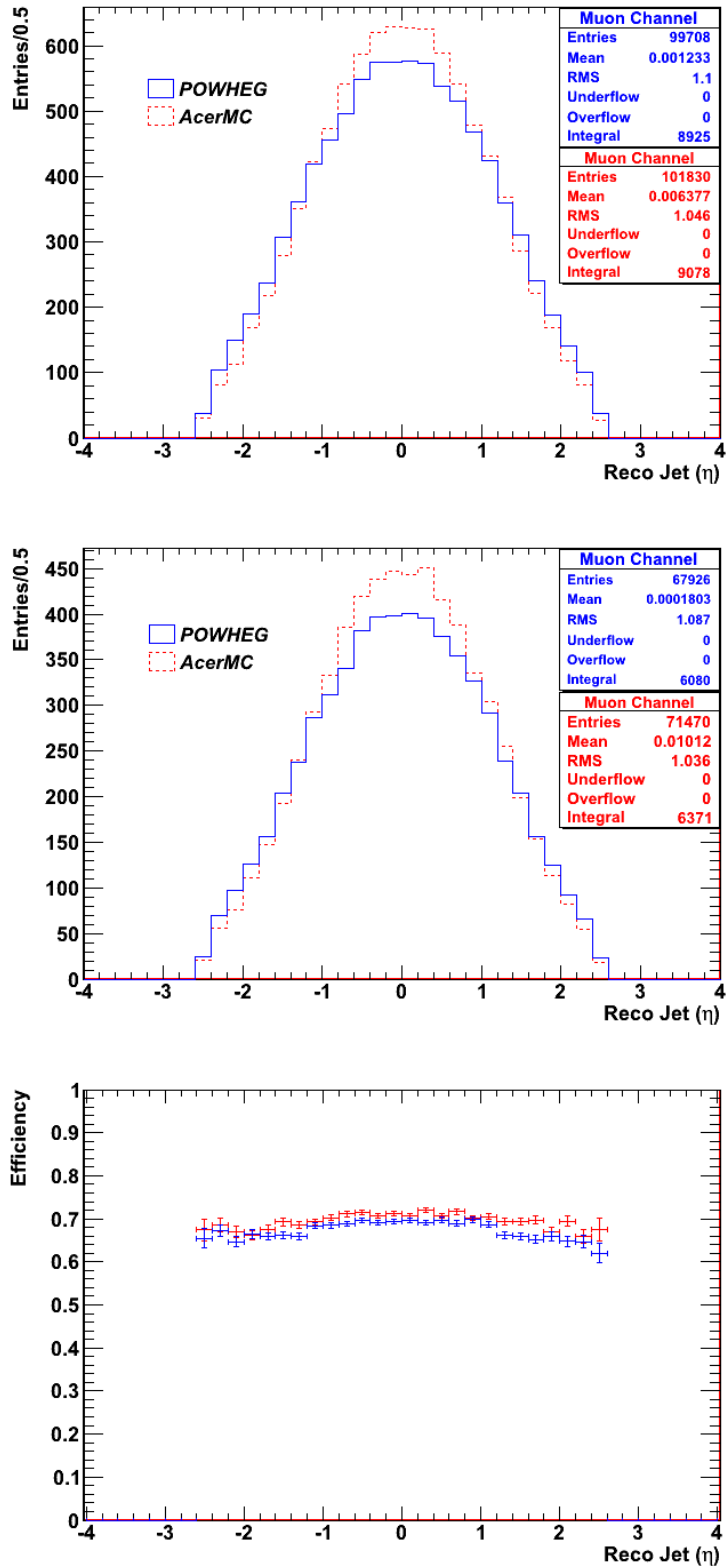
5.4 POWHEG+Pythia and MC@NLO+Herwig

Due to the reasons explained in the analysis strategy, the second step of the analysis involves a comparison between samples generated with POWHEG+Pythia and MC@NLO+Herwig. As pointed out earlier, both POWHEG and MC@NLO are next-to-leading order generators. The main goal here is to compare different parton shower models, Pythia and Herwig. Theoretical differences related to the handling of physical phenomena were described in Chapter 4. In this section, these differences will be observed directly comparing the kinematic distributions of physical observables.

The event selection strategy is exactly the same as in the Section 5.3. By the use of the same cut-based and geometrical matching selection, object efficiencies are obtained as a function of p_T and η. Then the relative difference of the efficiencies is calculated.

5.4.1 Leptons

In Figure 5.11, the upper and middle histograms show the transverse momentum distributions of true and reconstructed electrons, respectively. Distributions are shown for POWHEG + Pythia and MC@NLO + Herwig. The lower histogram shows the efficiency as a function of p_T. In Figure 5.12, the first and second histograms show the pseudorapidity distributions of the true and the reconstructed electrons, respectively. As in the first step of the analysis, except for the p_T cut at 25 GeV for reconstructed electrons due to the event selection, only minor differences can be seen in the distributions:

- The p_T distributions (Figure 5.11) for POWHEG + Pythia are slightly harder than MC@NLO + Herwig, both for true and reconstructed electrons. This is more prominent in the true p_T distribution.

- As a consequence of having a harder p_T distribution, the η distributions for the POWHEG + Pythia are expected to be narrower than those of MC@NLO + Herwig, as can be observed in Figure 5.12.

Besides the kinematic distributions of the electrons, the kinematic distributions of the muons are shown for POWHEG + Pythia and MC@NLO + Herwig with similar differences in Figures 5.13 and 5.14.

The efficiencies for the single electron and single muon selection are given in Table 5.5. The essential difference here is that the electron efficiency for MC@NLO is lower than the muon efficiency, while for POWHEG it is other way around. The relative differences between the efficiencies are shown in Table 5.6.

Figure 5.11: The upper histogram shows the p_T distribution of true electrons before all cuts for POWHEG + Pythia and MC@NLO + Herwig. The second one shows the p_T distribution of reconstructed electrons selected after the last lepton cut and truth matching. The lower histogram shows the efficiencies for the electron selection for the two samples.
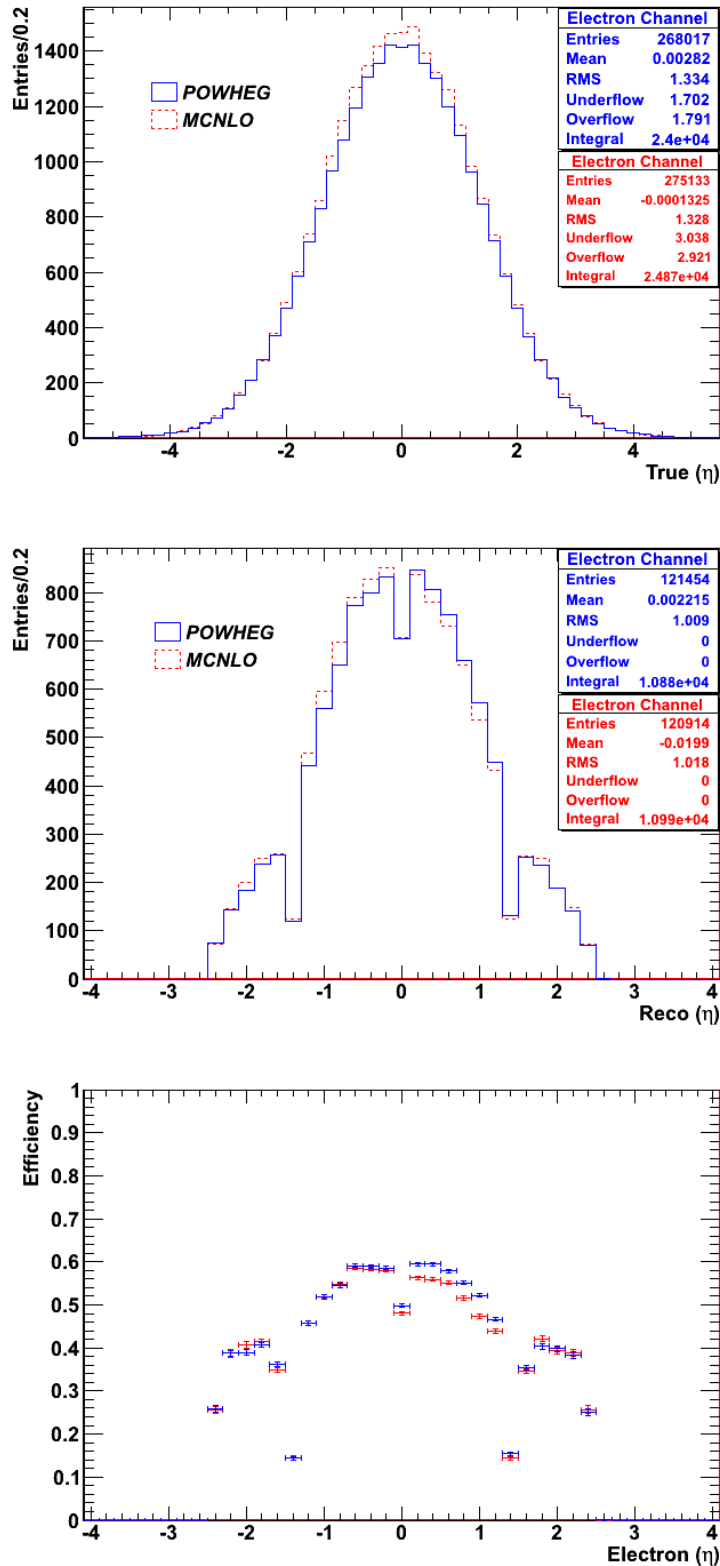
Figure 5.12: The upper histogram shows the η distribution of true electrons before all cuts for POWHEG + PYTHIA and MC@NLO + Herwig. The second one shows the η distribution of reconstructed electrons selected after the last lepton cut and truth matching. The lower histogram shows the efficiencies for the electron selection for the two samples.
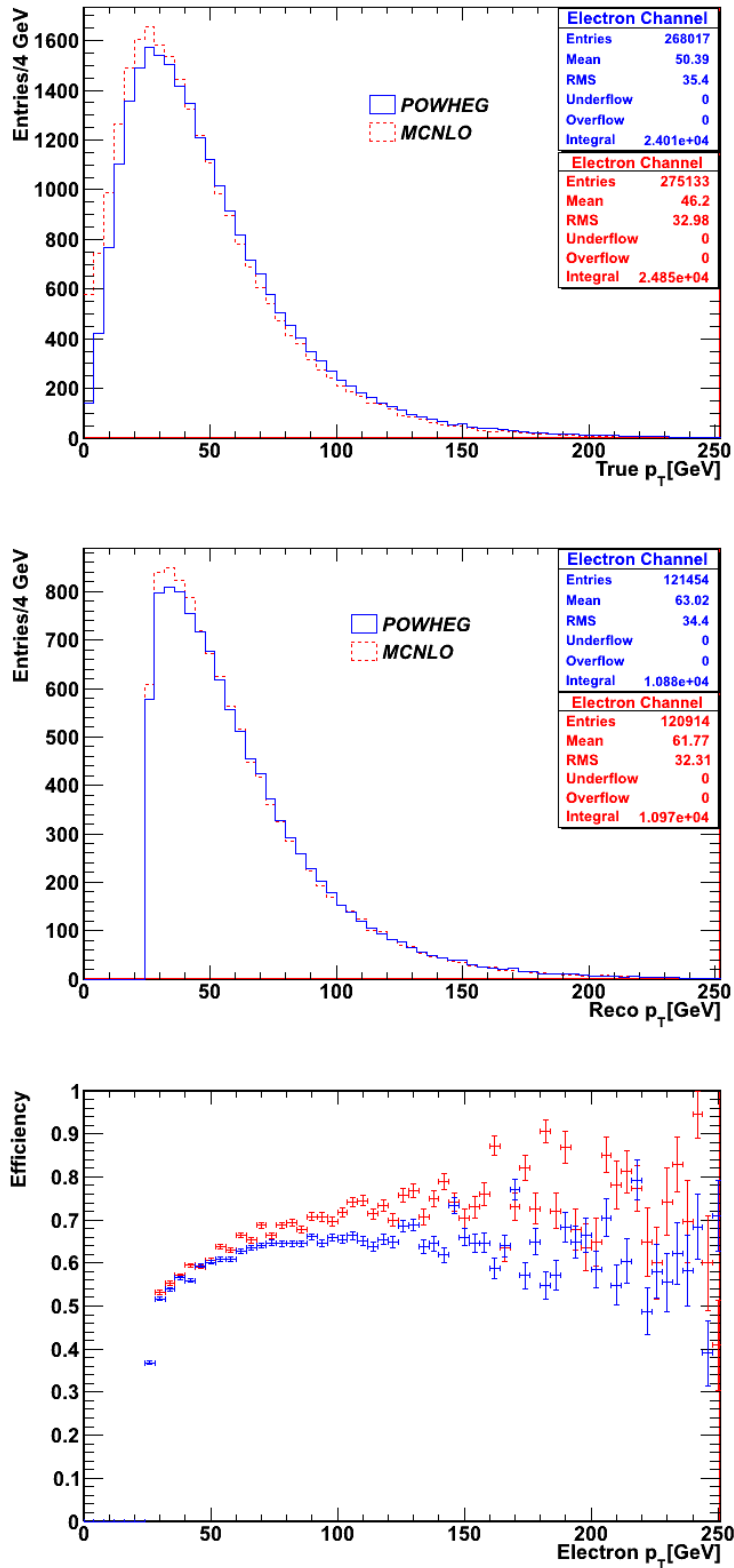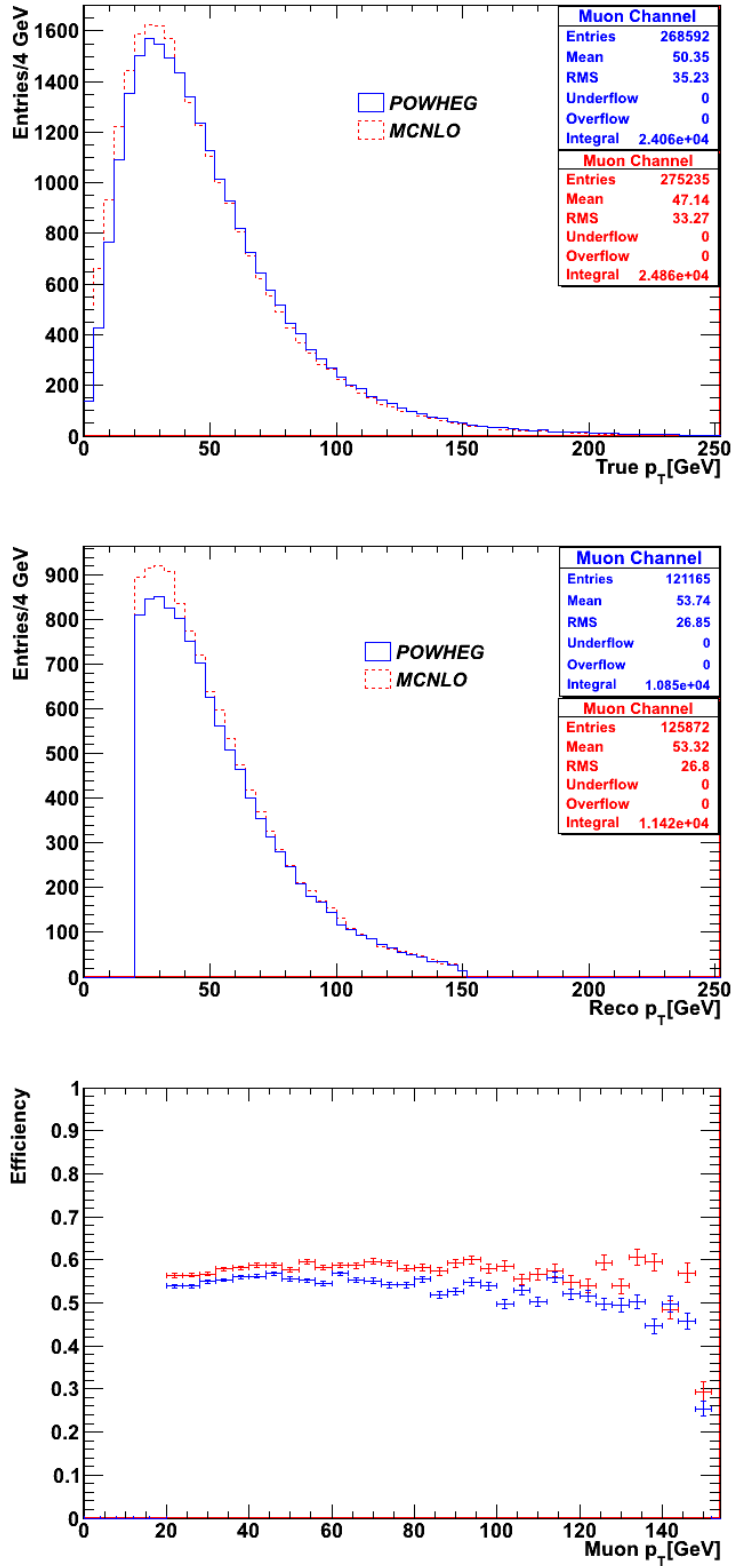
Figure 5.13: The upper histogram shows the p_T distribution of true muons before all cuts for POWHEG + PYTHIA and MC@NLO + Herwig. The second one shows the p_T distribution of reconstructed muons selected after the last lepton cut and truth matching. The lower histogram shows the efficiencies for the muon selection for the two samples.

Figure 5.14: The upper histogram shows the η distribution of true muons before all cuts for POWHEG + Pythia and MC@NLO + Herwig. The second one shows the η distribution of reconstructed muons selected after the last lepton cut and truth matching. The lower histogram shows the efficiencies for the muon selection for the two samples.
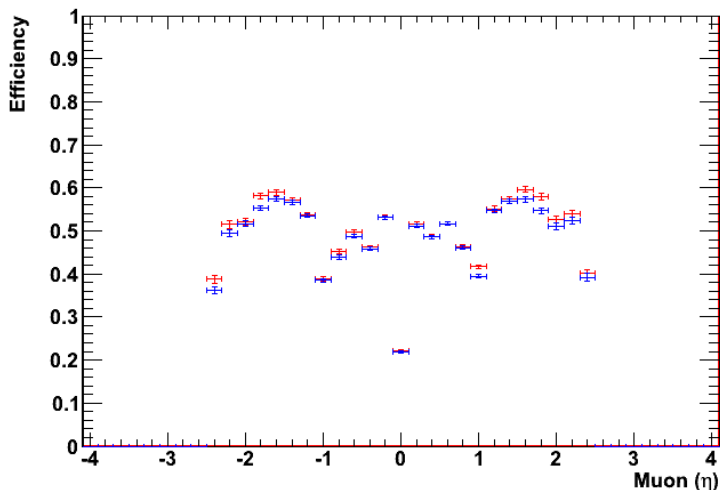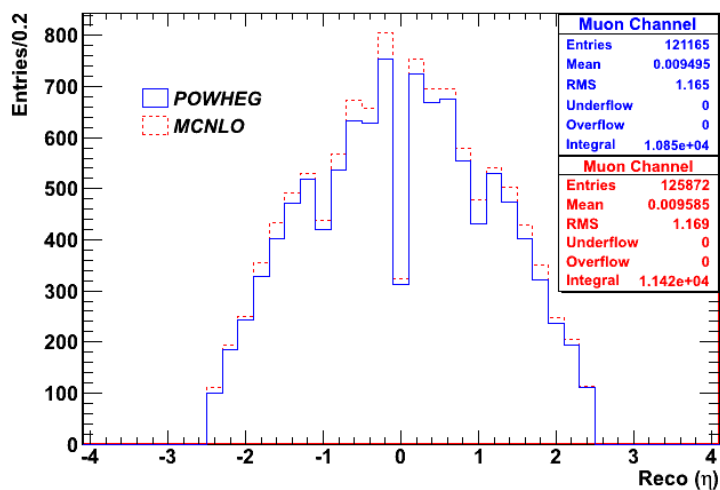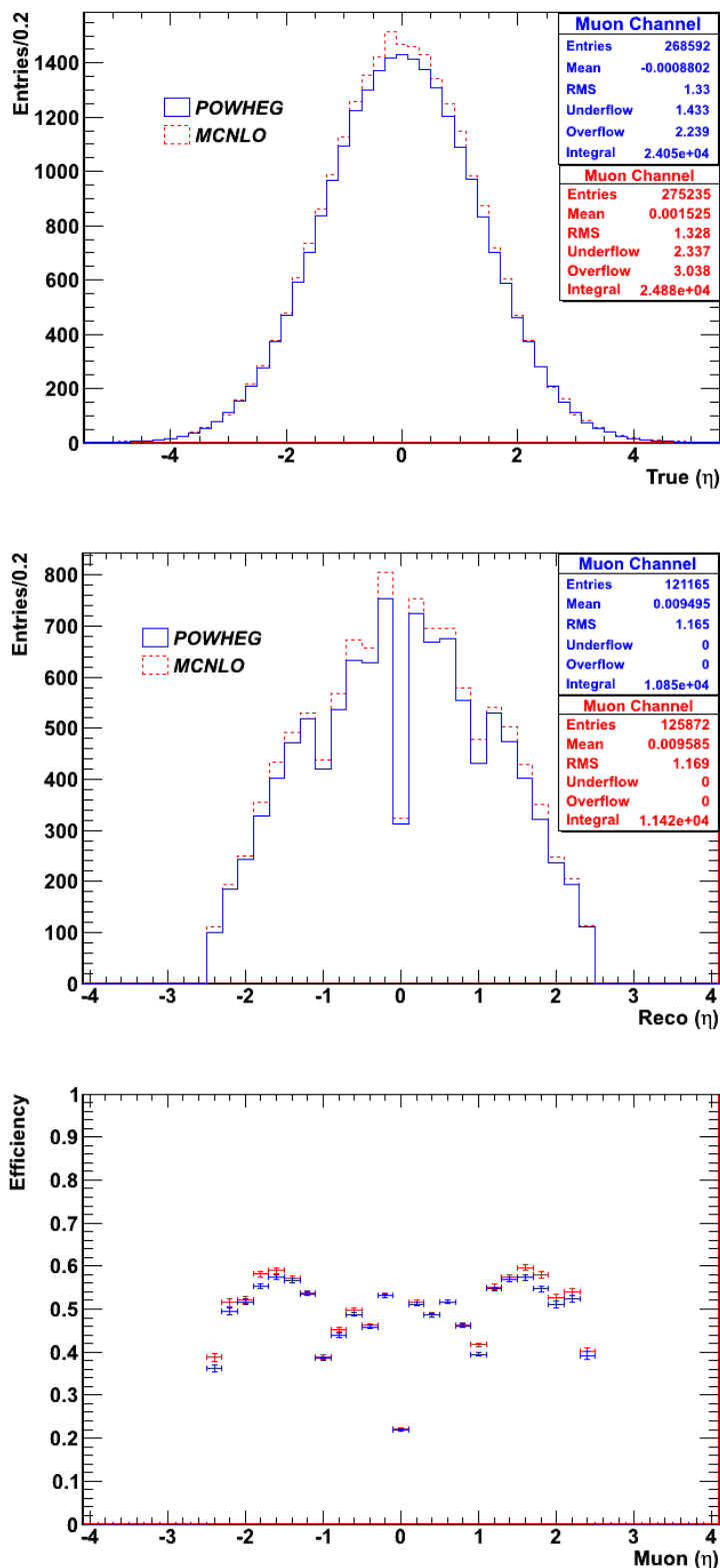
Table 5.5: Lepton Efficiencies For AcerMC and POWHEG MC Samples

	POWHEG	MC@NLO
e Channel	0.453±0.003	0.441±0.003
μ Channel	0.451±0.003	0.458±0.003

Table 5.6: Relative Difference of Lepton Efficiencies

	MC@NLO-POWHEG
e Channel	0.025±0.010
μ Channel	0.017±0.010

5.4.2   Jets

This section gives the results of the comparison of the jet efficiencies for POWHEG + Pythia and MC@NLO + Herwig. The kinematic distributions for jets can be seen in Figures 5.15, 5.16, 5.17 and 5.18. As for the kinematic distributions of the leptons in the previous section, POWHEG + Pythia has harder distributions compared to MC@NLO + Herwig. The calculated efficiencies are presented in Tables 5.7 and the relative difference between the efficiencies in Table 5.8.

Table 5.7: Jet Efficiency For POWHEG + Pythia and MC@NLO + Herwig

	POWHEG	MC@NLO
e Channel	0.657±0.006	0.649±0.006
μ Channel	0.681±0.005	0.671±0.005

Table 5.8: Relative Difference of the Jet Efficiencies

	MC@NLO-POWHEG
e Channel	0.012±0.012
μ Channel	0.014±0.010

Figure 5.15: The upper histogram shows the p_T distribution of reconstructed jets in the e^-+jets channel before the cut C12 for POWHEG + PYTHIA and MC@NLO + Herwig. The second one shows the p_T distribution of reconstructed jets after cut C14. The lower histogram shows the efficiencies for the jet selection for the two samples.
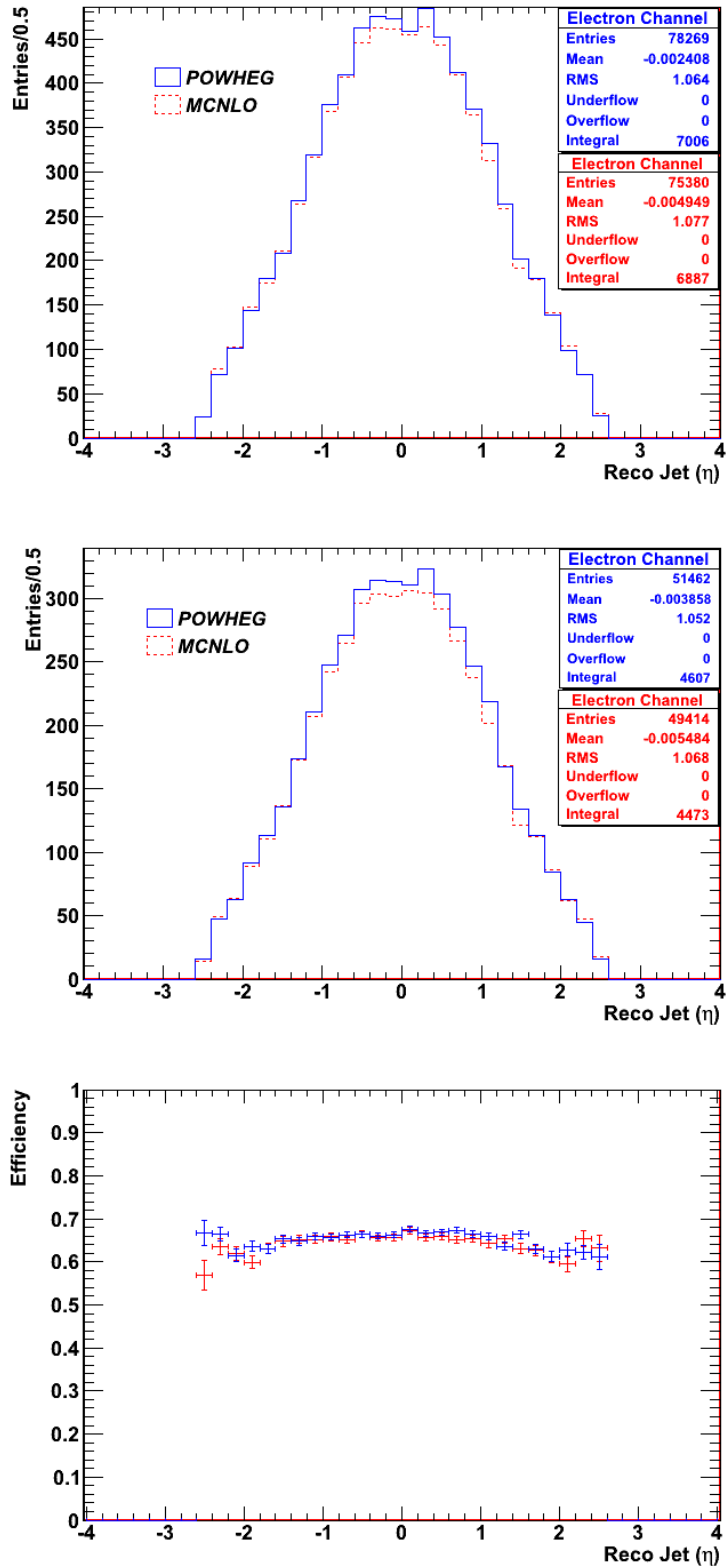
Figure 5.16: The upper histogram shows the η distribution of reconstructed jets in the e^-+jets channel before the cut C12 for POWHEG + PYTHIA and MC@NLO + Herwig. The second one shows the η distribution of reconstructed jets after cut C14. The lower histogram shows the efficiencies for the jet selection for the two samples.
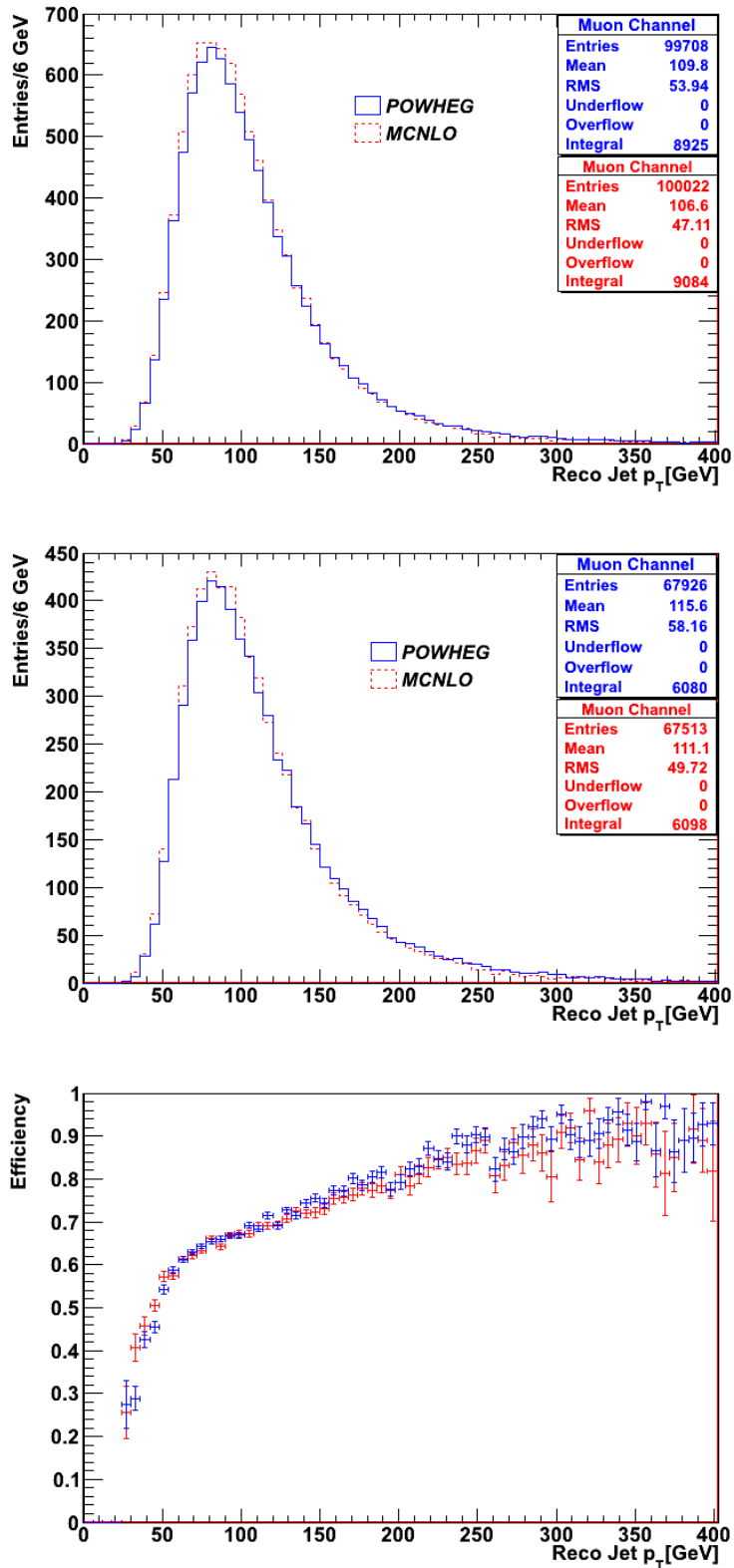
Figure 5.17: The upper histogram shows the p_T distribution of reconstructed jets in the μ+jets channel before the cut C12 for POWHEG + PYTHIA and MC@NLO + Herwig. The second one shows the p_T distribution of reconstructed jets after cut C14. The lower histogram shows the efficiencies for the jet selection for the two samples.
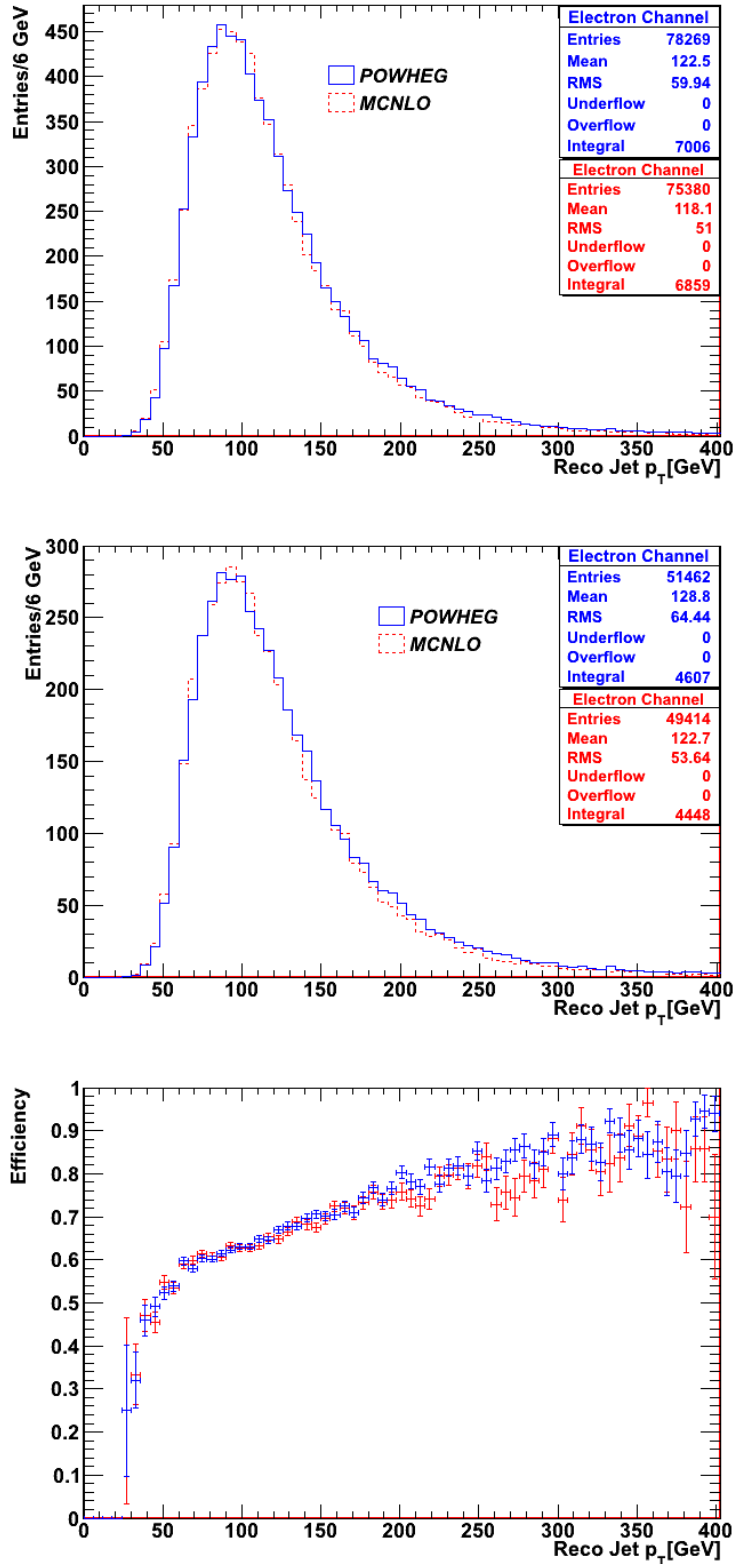
Figure 5.18: The upper histogram shows the η distribution of reconstructed jets in the μ+jets channel before the cut C12 for POWHEG + PYTHIA and MC@NLO + Herwig. The second one shows the η distribution of reconstructed jets after cut C14. The lower histogram shows the efficiencies for the jet selection for the two samples.
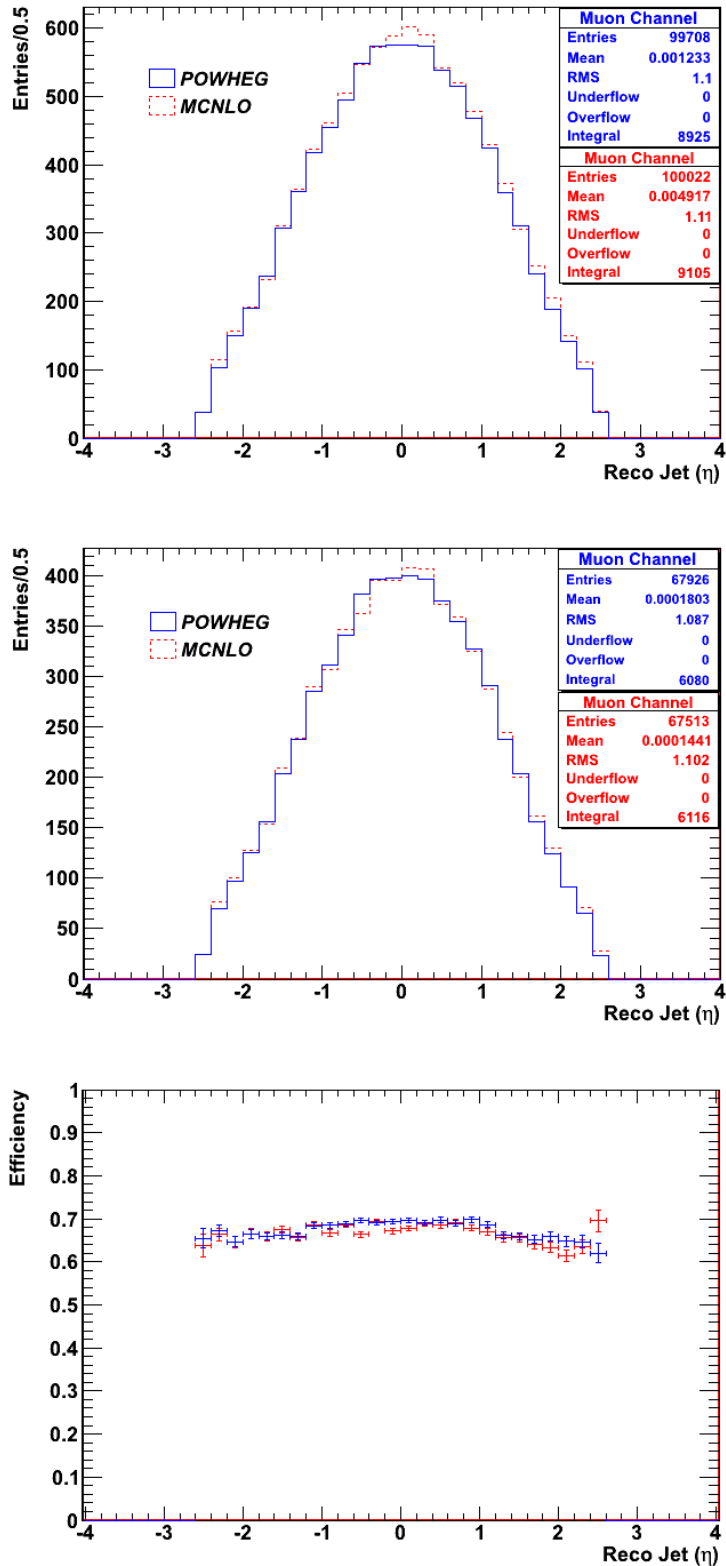
5.5 Final Results

The uncertainties determined in Sections 5.3 and 5.4 are summarized in Table 5.9. For leptons, the systematic uncertainty is between 1.0% and 2.5%, and for jets, the systematic uncertainty is between 1.2% and 2.9%. One has to note that the statistical uncertainty on these numbers is around 1.0% which is only slightly smaller than the uncertainties themselves. In order to have a total value as a final result, the uncertainty for leptons and the uncertainty for jets are summed up quadratically due to the following formula;

$$\sigma_{LO-NLO}^{Sum} = \sqrt{(\sigma_{LO-NLO}^{lepton})^2 + (\sigma_{LO-NLO}^{jet})^2} \qquad (5.4)$$

where σ_{LO-NLO}^{lepton} is the uncertainty due to LO and NLO comparison for leptons, σ_{LO-NLO}^{jet} is the uncertainty due to LO and NLO comparison for jets. The summation is done separately for electron and muon channels. The procedure is the same for NLO and NLO comparison. The quadratic summation is shown in Table 5.9.

Table 5.9: Systematic uncertainties for the efficiency in percent for AcerMC&POWHEG(LO-NLO) and Herwig&PYTHIA(NLO-NLO) comparisons with their quadratic summations for each channel separately.

		$\sigma_{LO-NLO}(\%)$	$\sigma_{NLO-NLO}(\%)$
Leptons	e Channel	1.7±1.0	2.5±1.0
	μ Channel	1.0±1.0	1.7±1.0
Jets	e Channel	2.6±1.2	1.2±1.2
	μ Channel	2.9±1.0	1.4±1.0
σ_{Sum}	e Channel	3.1±1.0	2.8±1.0
	μ Channel	3.1±0.9	2.2±1.0

At the end of the analysis, the final results are compared with the numbers calculated with respect to the cuts C0 and C14. Namely, the selection efficiencies due to these cuts are calculated in the previous cases (Sections 5.3 and 5.4). In order to calculate these numbers, the uncertainty due to C14 and C0 is calculated implementing both lepton and jet selection strategies together. After calculating the selection efficiency for each sample with respect to C0 and C14, the relative difference of these efficiencies are calculated. These number are then compared with the quadratic summation of the uncertainties calculated above. The efficiency calculation in this case includes all cuts from C1 upto C14. On the other side, the lepton selection efficiency calculation involves the cuts up to C7 and the jet selection efficiency calculation involves the cuts between C11 and C14, which means the cuts C8, C9, C10 and C11 are excluded. But these cuts affect the overall(C0-C14) efficiency

calculation and this can be the reason for any possible discrepancy in the comparison of the numbers. The results are shown in Table 5.10. Except the electron channel in

Table 5.10: Comparison of final results with the uncertainty calculated due to the overall(C0-C14) efficiency.

		σ_{Sum}	$\sigma_{C14/C0}$
LO&NLO	e Channel	3.1±1.0	3.3±1.6
	μ Channel	3.1±0.9	2.4±1.4
NLO&NLO	e Channel	2.8±1.0	1.2±1.6
	μ Channel	2.2±1.0	1.3±1.4

the comparison of LO and NLO samples the numbers calculated due to the cuts C0 and C14 are smaller than the quadratic sum of uncertainties. The reason for that can be the effects of the other cuts. A situation can be possible where the effects of the cuts, C8 C9, C10 and C11 have a negative or positive effect on the uncertainty calculated due to the overall(C0-C14) efficiency. Depending on this effect a smaller or bigger uncertainty can be expected compared to the quadratic sum uncertainties calculated due to the leptons and jet selection efficiencies.

Chapter 6

Summary and Outlook

The aim of this thesis was the determination of a systematic uncertainty for the measurement of the $t\bar{t}\gamma$ cross section, which is originating from the different handling of physical phenomena in leading order and next-to-leading order Monte Carlo simulations. Since a next-to-leading order $t\bar{t}\gamma$ sample does not exist, $t\bar{t}$ samples were compared to determine the uncertainty. For the comparison of different order generators, AcerMC + PYTHIA and POWHEG + PYTHIA were used. As a second systematic uncertainty two different models for parton showers were compared, POWHEG+PYTHIA and MC@NLO + Herwig. In the latter case, both, the event generator and the parton shower model were changed at the same time. However, one does not expect a large effect by using two different event generators when comparing parton showers, since the $t\bar{t}$ final states are well described at NLO level.

The uncertainties were determined separately for the leptons and for the jets in the final states. In all cases the uncertainties were around 2%, but with a large statistical uncertainty of 1% absolute. The uncertainties are also similar for the electron channel and the muon channel. In total, the uncertainty from the comparison of LO and NLO is 3.1±1.0% and the uncertainty from the parton shower model is 2.5±1.0%. In order to improve the statistical uncertainty on these numbers larger Monte Carlo samples are needed.

Bibliography

[1] P. W. Higgs: *Broken Symmetries, Massles Particles and Gauge Fields*. Phys. Lett. **12** (1964) 132.

[2] P. W. Higgs: *Broken Symmetries and the Masses of Gauge Bosons*. Phys. Lett. **13** (1964) 508.

[3] M. Kobayashi and T. Maskawa: *CP-Violation in the Renormalizable Theory of Weak Interactions*. Prog. Theor. Phys. **49** (1973) 652.

[4] A. Scharf K. Melnikov, M. Schulze: *QCD Corrections to Top Quark Pair Production in Association with a Photon at Hadron Colliders*. Phys. Rev. D **83**, 074013, 2011.

[5] CERN. Incident in LHC sector 3-4. Press Release PR09.08. http://public.web.cern.ch/press/pressreleases/Releases2008/PR09.08E.html.

[6] CERN. The LHC is back. Press Release PR16.09. http://public.web.cern.ch/press/pressreleases/Releases2009/PR16.09E.html.

[7] CERN.Two circulating beams bring first collisions in the LHC. Press Release PR17.09. http://public.web.cern.ch/press/pressreleases/Releases2009/PR17.09E.html.

[8] Ronald S. Moore Stephen Holmes and Vladimir Shiltsev: *Overview of the Tevatron Collider Complex: Goals, Operations and Performance*. 2011 JINST 6 T08001.

[9] CERN. CERN announces LHC to run in 2012. Press Release PR01.11. http://public.web.cern.ch/press/pressreleases/Releases2011/PR01.11E.html.

[10] CERN Accelerator Complex. http://public.web.cern.ch/public/en/research/AccelComplex-en.html.

[11] O. S. Bruening: *LHC Design Report*. http://cdsweb.cern.ch/record/782076, 2004.

[12] ATLAS Collaboration: *The ATLAS Experiment at the CERN Large Hadron Collider*. 2008 JINST 3 S08003.

[13] ALICE Collaboration: *The ALICE experiment at the CERN LHC.* 2008 JINST 3 S08002.

[14] CMS Collaboration: *The CMS experiment at the CERN LHC.* 2008 JINST 3 S08004.

[15] The LHCb Collaboration: *The LHCb Detector at the LHC.* 2008 JINST 3 S08005.

[16] J. W. Houston J. M. Campell and W. J. Stirling: *Hard Interactions of Quarks and Gluons: A Primer for LHC Physics.* http://arxiv.org/pdf/hep-ph/0611148, 2006.

[17] Donald H. Perkins: *Introduction to High Energy Physics.* Addison-Wesley Publishing Company, Inc., 1987.

[18] ATLAS Collaboration: *ATLAS Inner Detector: Technical Design Report Vol.1.* CERN-LHCC-97-016, http://cdsweb.cern.ch/record/331063, 1997.

[19] ATLAS Collaboration: *ATLAS Pixel Detector: Technical Design Report.* CERN-LHCC-98-013, http://cdsweb.cern.ch/record/381263, 1998.

[20] ATLAS Collaboration: *ATLAS Liquid-Argon Calorimeter: Technical Design Report.* CERN-LHCC-96-041, http://cdsweb.cern.ch/record/331061, 1996.

[21] ATLAS Collaboration: *ATLAS Muon Spectrometer: Technical Design Report.* CERN-LHCC-97-022, http://cdsweb.cern.ch/record/331068, 1997.

[22] I. Efthymiopoulos: *Overview of the ATLAS detector at LHC.* ATL-CONF-99-002, http://cdsweb.cern.ch/record/409257, May 1999.

[23] ATLAS Collaboration: *ATLAS Trigger Performance: Status Report.* CERN-LHCC-98-015, http://cdsweb.cern.ch/record/381430, 1998.

[24] F. Abe *et al.*: *Observation of Top Quark Production in $p\bar{p}$ Collisions with the Collider Detector at Fermilab.* Phys. Rev. Lett. **74** (1995) 2626 arXiv:hep-ex/9503002v2.

[25] S. Abachi *et al.*: *Observation of the Top Quark.* Phys. Rev. Lett. **74** (1995) 2632 arXiv:hep-ex/9503003v1.

[26] Arnulf Quadt: *Top Quark Physics at Hadron Colliders.* Eur. Phys. J., C48:835-1000 http://arxiv.org/abs/hep-ph/0507207, 2006.

[27] Wikipedia: *Standard Model.* http://en.wikipedia.org/wiki/Standard_Model, Last modified on 21 September 2011 at 13:59.

[28] W. N. Cottingham and D. A. Greenwood: *An Introduction to the Standard Model of Particle Physics, Second Edition.* Cambridge University Press, 2007.

[29] F. Halzen and A. D. Martin: *Quarks and Leptons: An Introductory Course in Modern Particle Physics.* John Wiley Sons, Inc., 1984.

[30] O. Biebel: *Experimental Tests of the Strong Interaction And Its Energy Dependence in Electron-Positron Annihilation.* Phys. Rept. 340:165-289, 2001.

[31] D. Griffiths: *Introduction to Elementary Particles, Second Edition.* WILEY-VCH Verlag GmbH Co. KGaA, Weinheim, 2008.

[32] H. L. Lai *et al.*: *Global QCD Analysis of Parton Structure of the Nucleon: CTEQ5 Parton Distributions.* Eur. Phys. J., C **12**, 375 (2000) arXiv:hep-ph/9903282v3.

[33] Fermilab: *The Tevatron: 28 years of discovery and innovation.* http://www.fnal.gov/pub/tevatron/.

[34] Wolfgang Wagner: *Top quark physics in hadron collisions.* Rept. Prog. Phys., 68:2409-2494 arXiv:hep-ph/0507207v2.

[35] M. Buice U. Baur and L. H. Orr: *Direct Measurement of Top Quark Charge at Hadron Colliders.* Phys. Rev. D **64** (2001) 094019.

[36] The ATLAS Collaboration. ATLAS-CONF-2010-153, 2011.

[37] T. Gleisberg *et al*: *Event Generation with SHERPA 1.1.* JHEP **0902** 007, arXiv:0811.4622v1, 2009.

[38] T. Sjostrand: *Academic Training Lecture: Monte Carlo generators for the LHC, CERN.* http://cdsweb.cern.ch/record/794322/, April 2005.

[39] P. Skands T. Sjoestrand, S. Mrenna: Pythia *6.4 Physics and Manual.* arXiv:hep-ph/0603175, 2006.

[40] V. N. Gribov and L. N. Lipatov: *Deep Inelastic ep Scattering in Perturbation Theory.* Sov. J. Nucl. Phys. **15** (1972) 428.

[41] L. N. Lipatov: *The Parton Model and Perturbation Theory.* Sov. J. Nucl. Phys. **20** (1975) 94.

[42] G. Altarelli and G. Parisi: *Deep Inelastic ep Scattering in Perturbation Theory.* Nucl. Phys. B **126** (1977) 298.

[43] Y. Dokshitser: *Calculation of the Structure Functions for Deep Inelastic Scattering and electron-positron Annihilation by Perturbation Theory in Quantum Chromodynamics.* Sov. Phys. JETP Nucl. **46** (1977) 641.

[44] V. V. Sudakov: *Vertex Parts at Very High Energies in Quantum Electrodynamics.* Sov. Phys. JETP **30** (1956) 65.

[45] T. Sjoestrand and P. Skands: *Transverse-Momentum-Ordered Showers and Interleaved Multiple Interactions.* arXiv:hep-ph/0408302, 2004.

[46] G. Corcella and *et al*: *HERWIG 6.5 An event Generator for Hadron Emission Reactions with Interfering Gluons.* arXiv:hep-ph/0011363v3, 2002.

[47] J. R. Forshaw J. M. Butterworth and M .H. Seymour: *Multiparton Interactions in Photoproduction at HERA.* Z Phys. **C72** (1996) 637 arXiv:hep-ph/9601371.

[48] T. Sjostrand and P. Z. Skands: *Multiple Interactions and Structure of Beam Remnants.* JHEP **03** (2004) 053 arXiv:hep-ph/0402078.

[49] T. Sjostrand and P. Z. Skands: *Transverse-Momentum-Ordered Showers and Interleaved Multiple Interactions.* Eur. Phys. J. **C39** (2005) 129 arXiv:hep-ph/0408302.

[50] B. P. Kersevan and E. Richter-Was: *The Monte Carlo Event Generator AcerMC 2.0 with Interfaces to PYTHIA 6.2 and HERWIG 6.5.* arXiv:hep-ph/0405247v1, 2004.

[51] T. Stelzer and W. F. Long: *Automatic Genaration of Tree Level Helicity Amplitudes.* Comput. Phys. Commun. 81 (1994) 357.

[52] S. Frixione and B. R. Webber: *Matching NLO QCD Computations and Parton Shower Simulations.* arXiv:hep-ph/0204244v2, 2002.

[53] P. Nason S. Frixione and C. Oleari: *Matching NLO QCD Computations with Parton Shower Simulations: The POWHEG Method.* JHEP **11** (2007) 070 arXiv:hep-ph/0709.2092v1, 2007.

[54] P. Nason S. Frixione and G. Ridolfi: *A Positive-Weight Next-to-Leading Order Monte Carlo for Heavy Flavour Hadroproduction.* JHEP **09** (2007) 126 arXiv:hep-ph/0707.3088v3, 2002.

[55] P. Nason S. Frixione and G. Ridolfi: *The POWHEG-hvq Manual Version 1.0.* arXiv:hep-ph/0707.3081v1, 2009.

[56] ATLAS Collaboration: *The ATLAS Computing Workbook.* https://twiki.cern.ch/twiki/bin/viewauth/Atlas/WorkBookFullChain.

[57] A. Dellacqua *et al*: *GEANT4: An Object Oriented Toolkit For Simulation in HEP.* CERN-DRDC-94-29, 1994.

[58] ATLAS Collaboration: *ATLAS Computing: Technical Design Report.* CERN-LHCC-2005-022, http://cdsweb.cern.ch/record/837738, 2005.

[59] ATLAS Collaboration: *ATLAS Letter of Intent for a General Purpose pp Experiment at the Large Hadron Collider at CERN.* CERN/LHCC/92-4, 1992.

[60] K. Cranmer: *The ATLAS Analysis Architecture*. Nucl. Phys. B, Proc. Suppl. 177-178 126-130 http://cdsweb.cern.ch/record/1047631, 2008.

[61] K. Koeneke *et al*: *A new data format for the commissioning phase of the ATLAS detector*. J. Phys.: Conf. Ser., vol. 219, 032047, 2010.

[62] Peng Fei Duan *et. al.* Phys. Rev. D **80**, 014022, 2009.

[63] O. Arnaez on behalf of the ATLAS Collaboration: *Electron Reconstruction and Identification with the ATLAS Detector*. ATLAS-PHYS-PROC-2009-118, http://cdsweb.cern.ch/record/1209898, 2009.

[64] B. Resende on behalf of the ATLAS Collaboration: *Muon Identification Algorithms in ATLAS*. ATLAS-PHYS-PROC-2009-113, http://cdsweb.cern.ch/record/1209632, 2009.

[65] G. P. Salam M. Cacciari and G. Soyez: *The Anti-kt Jet Clustering Algorithm*. JHEP04 (2008) 063.

[66] W. Lampl *et al*: *Calorimeter Clustering Algorithms: Description and Performance*. JHEP04 (2008) 063, http://iopscience.iop.org/1126-6708/2008/04/063.

[67] *et al.* S. Catani: *Longitudinally Invariant K(t) Clustering Algorithms for Hadron Hadron Collisions*. Nucl. Phys. **B 406** (1993) 187.

[68] S. D. Ellis and D.E. Soper: *Successive Combination Jet Algorithm for Hadron Collisions*. Phys. Rev. **D 48** (1993) 3160 arXiv:hep-ph/9305266.

[69] Y. L. Dokshitzer *et al.*: *Better Jet Clustering Algorithms*. JHEP **08** (1997) 001 arXiv:hep-ph/9707323.

[70] M. Wobisch and T. Wengler: *Hadronization Corrections to Jet Cross Sectionsin Deep-Inelastic Scattering*. arXiv:hep-ph/9907280.

[71] D. Olivito M. Hance and H. Williams: *Performance Studies for e/gamma Calorimeter Isolation*. ATL-COM-PHYS-2011-1186, http://cdsweb.cern.ch/record/1379530, 2011.

[72] https://twiki.cern.ch/twiki/bin/viewauth/AtlasProtected/ElectronIdentification.

[73] https://twiki.cern.ch/twiki/bin/viewauth/AtlasProtected/TopCommonObjects.

[74] *Private Communication with Liza Mijovic*, 15.04.2011.

[75] https://twiki.cern.ch/twiki/bin/viewauth/AtlasProtected/HowToCleanJets#Bad_jets.

[76] G. Cowan: *Error Analysis for Efficiency*, 2008.

[77] https://twiki.cern.ch/twiki/bin/viewauth/AtlasProtected/TopCommonObjects#Muon_trigger_matching.

Acknowledgements

With the submission of my thesis, I would like to thank the people who supported and helped me during with my master thesis.

I would like to thank first *Prof. I. Fleck* for giving me the chance to work within a very interesting project, ATLAS Experiment as well as for believing in my excitement for further research. I thank also;

Marcus Rammes, for his helps in many aspects throughout my thesis.

Hendrik Czirr, for his time to read my thesis and for suggestions.

Oliver Rosenthal, for his comments at critical points and for his help during the thesis.

Andreas Weikum, for being a close friend and for the times we had happy-hour cocktails besides a warm conversation.

Christian Hachenberg, for the good time we had together at CERN.

Ugur Senlik, for his true friendship, for standing by me during the hard times, and for sharing problems we faced together.

I would specially thank my family for supporting me at every moment of my life and for trying to do best for me and my brother. At last, thank you *Semos*, for your invaluable love, help and support.

Datum   Unterschrift

Erklärung

Hiermit verschiere ich, dass ich die vorliegende Masterarbeit selbstständig verfasst und keiene anderen als die angegebenen Quellen und Hilfsmittel benuzt, sowie Zitate und Ergebnisse Anderer kenntlich gemacht habe.

Datum   Unterschrift